Supplementary Materials for

Spatiotemporal visualization of CO_2 electrolysis

Xin Lu[1†], Chris Zhou[2†], Roxanna S. Delima[2,3], Eric W. Lees[3], Abhishek Soni[1], David J. Dvorak[2], Shaoxuan Ren[1], Tengxiao Ji[1], Addie Bahi[2], Frank Ko[2*] & Curtis P. Berlinguette[1,2,3,4,*]

Correspondence to: cberling@chem.ubc.ca

This PDF file includes:

Other Supplementary Materials for this manuscript include the following:

Movies S1 to S8

S0. Movie captions

Movie S1. Time-resolved visualization of the electrolysis optical coherence tomography (eOCT) intensity in the X–Z plane of the CO_2 electrolyzer during 12 h of electrolysis at 100 mA cm^{-2}.

Movie S2. 3D rotational view of the cathode captured by electrolysis optical coherence tomography (eOCT) during electrolysis at a current density of 100 mA cm^{-2}.

Movie S3. Time-resolved visualization of the electrolysis optical coherence tomography (eOCT) intensity in the X–Z plane of the CO_2 electrolyzer when the current density is switched from 0 to 100 mA cm^{-2}. Bubbles are formed at the membrane and cathode which causes separation of the two layers during electrolysis.

Movie S4. Time-resolved visualization of electrolysis optical coherence tomography (eOCT) of a control experiment used to quantify CO_2 bubbles.

Movie S5. Time-resolved visualization of the electrolysis optical coherence tomography (eOCT) intensity in the X–Z plane of the CO_2 electrolyzer of single CO_2 bubble dynamics at the membrane surface at a current density of 100 mA cm^{-2}. This movie tracks the classical bubble evolution microprocesses including nucleation, necking, and collapse.

Movie S6. Time-resolved visualization of the electrolysis optical coherence tomography (eOCT) polarization in the X–Z plane of the CO_2 electrolyzer of single CO_2 bubble dynamics at the membrane surface at a current density of 100 mA cm^{-2}. This movie tracks the classical bubble evolution microprocesses including nucleation, necking, and collapse.

Movie S7. The phase-distribution movie showing the presence of $CO_{2(g)}$ pathway at the cathode, continuously supplying $CO_{2(g)}$ to form $CO_{(g)}$.

Movie S8. The signal similarities between reactants and products for CO2RR and HER with time shifts applied.

S1. Materials and Methods

S1A. Fabrication and characterization of the cathode

Materials

Polyvinylidene fluoride (PVDF, average M_w ~275,000), dimethylformamide (DMF, ≥99%), acetone (≥99.5%, ACS reagent grade), polyvinylpyrrolidone (PVP), silver nanoparticles (99.5% trace metals basis), and ethylenediaminetetraacetic acid (EDTA, 99%) were purchased from Sigma Aldrich. $KHCO_3$ (99.9%) was purchased from Alfa Aesar. Nickel foam (>99.99%) was purchased from MTI Co. Fumasep-FBM® bipolar membranes were purchased from Fuel Cell Store and stored in a NaCl solution (1 M) prior to use. N_2 (99%), CO_2 (99%) and Ar (99.999%) gases were purchased from Praxair Canada Inc.

Fabrication

The cathode was fabricated using electrospinning, a technique for making continuous ultralong nanofibers at low cost and in large quantities (*1*, *2*). PVDF (20 wt.%) was dissolved in 3:2 acetone:DMF in volume ratio. The Ag nanoparticles were dispersed in this acetone/DMF solvent at a concentration of 34 mg mL^{-1} using a reported ultrasonication method (*3*). The distance between the electrospinning needle and the substrate on the drum collector was 15 cm. A voltage of 15 kV was used and the PVDF solution was pumped through the needle at a flow rate of 0.02 mL min^{-1}. To ensure uniformity of the nanofibers, the syringe was mounted onto a motor-driven platform that scans tangentially to the drum collector with a speed of 10 cm min^{-1}. The sample was heated overnight to ensure all solvents had evaporated and was then hot pressed at 105 °C. 350 nm of silver was deposited onto the nanofibers using an Angstrom Engineering deposition system.

Multi-jet electrospinning

A multi-jet electrospinning process was used to fabricate the cathode from one jet for PVDF and another jet for PVP. The electrospinning parameters of the PVDF jets were set the same as shown in the fabrication of the cathode. PVP (10 wt.%) in ethanol was pumped through the jet under a voltage of 15 kV at the 0.02 mL min^{-1} flow rate. The nanofibers were then dipped into water to remove the PVP. The Ag electrocatalyst of the same thickness was deposited onto the nanofibers using sputtering. The thicknesses of the porous cathodes were controlled by the electrospinning time (*1*, *2*). To control pore size while maintaining nanoscale fiber diameter, we adjusted the fraction of PVP from 0–50% prior to multi-jet electrospinning.

Characterization

Scanning electron microscopy (SEM) was carried out using an FEI Helios NanoLab 650 dual beam SEM. For imaging, the accelerating voltage was set to 1 kV, and the current was set to 50 pA. Energy dispersive X-ray (EDX) maps of size 256 × 200 pixels were collected at 10 kX magnification using an accelerating voltage of 10 kV and beam current of 0.80 nA.

S1B. Flow cell design

All electrolysis optical coherence tomography (eOCT) measurements were performed using a custom-designed and built zero-gap flow cell reactor consisting of housings, gaskets, anode flow-field plates and cathode flow-field plates with a transparent window, and a membrane electrode assembly (MEA; Fig. 1, S1). The MEA (geometric surface area = 4 cm^2) was assembled with a nickel foam anode, a bipolar membrane, and a porous cathode. The cathode was prepared by electrospinning polymer solution with silver (Fig. S3, S4). The stainless steel anode and cathode housings (6 × 6 × 1.2 cm) served to deliver liquids to the anode and cathode, respectively, through ⅛″ national pipe taper (NPT) ports with barbed tubing adapters. A grade 2 titanium cathode flow-

field plate with a small transparent window inserted in the middle and a stainless steel anode flow-field plate (316 stainless steel) sandwiched the MEA (Fig. S1). The anode and cathode flow-field plates (6 × 6 × 0.6 cm; geometric surface area = 4 cm^2) contained serpentine channels 1.5 mm wide and 1.5 mm deep with 1-mm ribs. This flow-field plate design has been previously reported (*4*). All gaskets were cut from 1.5-mm thick chemical resistant compressible polytetrafluoroethylene (PTFE). All flow cell components were chosen for their chemical inertness in basic and acidic conditions. In this flow cell, 1 M KOH and 3 M $KHCO_3$ solutions were provided to the anode and cathode compartments, respectively.

S1C. Electrochemical test procedure

Electrolysis and product analysis

During the electrolysis and imaging, the anode compartment of the cell was circulated with 1000 mL of 1.0 M KOH at a flow rate of 40 mL min^{-1}. The catholyte feed was 1000 mL of 3.0 M $KHCO_3$ with 0.02 M EDTA, delivered at various flow rates (20 to 110 mL min^{-1}) and recycled to a reservoir. The gas products were collected and quantified by gas chromatograph (GC). The GC was equipped with a packed MolSieve 5 A column and a packed HaySep D column. Argon (Praxair, 99.999%) was used as the carrier gas. The GC was calibrated by injecting different calibration gas mixes from NorLAB containing CO, CH_4, H_2, C_2H_4, C_2H_6, CO_2, and C_3H_8 at concentrations ranging from 100–50000 ppm. CO and H_2 were detected by a flame ionization detector (FID) and a thermal conductivity detector (TCD), respectively.

Electrochemical measurements were conducted at ambient conditions using a potentiostat (CH instruments 660D with a picoamp booster) through two-electrode cell measurements. Current density is calculated using the total current (mA) divided by the geometric surface area of the electrodes (4 cm^2). ^1H NMR analysis of the anolyte and catholyte reservoirs indicated that no liquid

products were formed in meaningful quantities (i.e., liquid CO2RR products accounted for <2% of all products formed). The faradaic efficiency (*FE*) of gaseous products was determined using the equation below (*5*):

$$FE = n_k F x_k F_m / I \quad \text{(Eq. S1)}$$

where n_k is the number of electrons per mole of gaseous product k involved in the reduction reaction, F is Faraday's constant (F = 96,485 C mol^{-1}), x_k is the mole fraction of gas k in the gaseous mixture analyzed using GC, F_m is the molar flow rate in mol s^{-1}, and I is the total current in A. The molar flow rate is derived from the volumetric flow rate F_v by the ideal gas law ($F_m = PF_v/RT$), where P is the atmospheric pressure in Pa, R is the ideal gas constant of 8.314 J mol^{-1} K^{-1}, and T is the temperature in K. Here the volumetric flow rate F_v was measured using a flow indicator located immediately at the inlet of the GC.

Salt crystallization and removal experiment

A control experiment performed using a clean electrolyzer (rinsed with deionized water) and recycled electrolyte (3.0 M $KHCO_3$) showed an increase in j_{CO} from 72 to 81 mA cm^{-2} after 5 min of electrolysis. These results suggest that any products and/or contamination at the cathode can cause a decrease in j_{CO} due to the salt formation issue. However, this issue can be mitigated by rinsing the cell with deionized water, consistent with previous reports (*5*).

S2. The design of the eOCT system for real-time, depth CO2RR observation

S2A. Light matrices measurement and analysis

Jones (*J*) and Mueller (M) matrices were used to study the light polarization properties (*6–8*) of the operational CO_2 electrolyzer micro-environment. A Jones matrix describes the response to fully-polarized light (Eq. S2). A Mueller matrix can extend the capability of a Jones matrix to describe the depolarization phenomena that come from multiple compositions (*9–12*).

$$J = \begin{bmatrix} j_{11} & j_{12} \\ j_{21} & j_{22} \end{bmatrix} \quad \text{(Eq. S2)}$$

Here *j* indicates the transfer elements of a Jones matrix. We derived the 4 × 4 covariance matrix $\boldsymbol{T}$ with ensemble averaging from Jones (*J*) matrices (*13*):

$$\boldsymbol{T} = \underline{\overline{\boldsymbol{\kappa}\boldsymbol{\kappa}^{\dagger}}} \quad \text{(Eq. S3)}$$

where $\boldsymbol{\kappa}$ denotes the vectorized *J* and the superscripted dagger denotes complex transpose.

The variations of inherent material properties were expressed by depolarization (*14*, *15*). The depolarization index P_{Δ} was defined as Eq. S4:

$$\boldsymbol{P}_{\Delta} = \frac{1}{\sqrt{3}}\sqrt{4\sum_{n=0}^{3}\hat{\lambda}_n^2 - 1} \qquad \left(\hat{\lambda}_n = \frac{\lambda_n}{Tr(T)}\right) \quad \text{(Eq. S4)}$$

where λ_n was the n^{th} eigenvalue of the matrix $\boldsymbol{T}$, and *Tr(T)* denotes a trace of the matrix $\boldsymbol{T}$. The 4 × 4 covariance matrix $\boldsymbol{T}$ was then converted to the Mueller (M) matrix (*16*). The eigenvalues of $\boldsymbol{T}$ were also utilized to modify the reconstructed M matrices to be physically acceptable Mueller matrices (*17–19*).

S2B. eOCT for imaging a CO_2 electrolyzer

The eOCT system

The basic design of the eOCT system followed the interferometer prototype in Ref. (*20*). To facilitate fast measurement, a tunable vertical-cavity surface emitting laser (VCEL, Thorlabs Inc., Newton, New Jersey, US) with a center wavelength of 1060 nm, a bandwidth of 111 nm, and a repetition rate of 100 kHz was selected as the light source. This laser was previously demonstrated in high-speed and long-range swept-source optical coherence tomography (OCT) imaging of biological tissue (*21, 22*). The interferometer was configured in a parallel-polarization detection mode (*23*) to measure all elements of the Jones matrix without compromising the top-down scan rate or the depth-encoded scan. A polarization-maintaining filter coupler (PMFC) splits the laser beam between the reference path and the CO_2 electrolyzer path. The incident beam was then directed through an optical window into the CO_2 electrolyzer. The scattered light was collected in another PMFC to distinguish the two orthogonal incident states of polarization. The scattering intensity signal obtained at each sampled wavelength demonstrated a 1:1 relationship with each physical position along the depth profile, which was valid for the entire detectable depth range (~2 mm) as described by partial coherence mechanism (*24*).

The detection mechanism

eOCT utilizes the nature of light, i.e. inherent wave properties, including frequency, phase, interference, and polarization. By detecting the clustering photons, one can achieve information multiplexing, which largely enhances the data collection efficiency in spatial, temporal, and functional domains, even near or below its resolution limit (defined by a point spread function, i.e. PSF) (*25*). Not only the imaging speed is increased, but also the polarization information is recorded simultaneously. The combination of partial coherence theory and the polarization

calculus does not rely on the extinction of the illuminating photons (like absorption in x-ray tomography), but fully utilizes the free-path of the random walking photons which pass through the materials and carry information. The capabilities of eOCT make it suitable for real-time detection of various multiphase chemical reactions in turbid media. In order to achieve these chemical maps in Fig. 4, we recorded the polarization information of clusters of photons for each local pixel at a rate of ~10 ns. As mentioned, for any information below the system resolution limit, the corresponding scattered photons can be readily collected with a blurring effect in the imaging space, which is equivalent to a broadening PSF. Such a PSF can be mathematically simplified as a Gaussian fitter (same as the probability mask for various phases but in the spatial domain).

S3. Methods for obtaining phase-distribution images

S3A. Theory

We used light polarization matrices to identify electrolyzer components. Light scattering, simultaneously allocated into different polarization matrix elements, was used to assess the properties of the complex and turbid medium of the aqueous electrolyzer. A depth-resolved Mueller matrix $\mathbf{M}(\boldsymbol{z})$ was used to describe sample depolarization and many other inherent optical properties that can be found by polar decomposition (*10*) and differential decomposition (Eq. S5) (*26*).

$$\frac{d\mathbf{M}(z)}{dz} = \boldsymbol{m}\mathbf{M}(z) \qquad \text{(Eq. S5)}$$

where $\boldsymbol{m}$ is the differential Mueller matrix that represents more detailed depth-resolved information about the depolarizing anisotropic properties (Eq. S6) which are associated with the spatiotemporal fluctuations of the media.

$$\boldsymbol{m} = \sum_{\boldsymbol{n=1}}^{\boldsymbol{16}} \boldsymbol{m_n} = \begin{bmatrix} \kappa_i & \kappa_q + \kappa'_q & \kappa_u + \kappa'_u & \kappa_v + \kappa'_v \\ \kappa_q - \kappa'_q & \kappa_i - \kappa'_{i,q} & \eta_v + \eta'_v & -\eta_u + \eta'_u \\ \kappa_u - \kappa'_u & -\eta_v + \eta'_v & \kappa_i - \kappa'_{i,u} & \eta_q + \eta'_q \\ \kappa_v - \kappa'_v & \eta_u + \eta'_u & -\eta_q + \eta'_q & \kappa_i - \kappa'_{i,v} \end{bmatrix} \qquad \text{(Eq. S6)}$$

The Cloude decomposition (*27*) of $\boldsymbol{m}$ produces its covariance matrix Σ, whose eigenvalues contribute to the differential depolarization index (DDI) (Eq. S7) (*25*).

$$DDI = ||\Sigma|| = \sqrt{Tr(\Sigma^{\dagger}\Sigma)} \qquad \text{(Eq. S7)}$$

where Σ is the covariance matrix and the superscripted dagger denotes complex transpose (*26*). The *DDI* is directly related to the variance and covariance of the anisotropic properties of the sample, which are proposed to quantify depolarization (*26*, *28*, *29*).

S3B. Methods for characterizing phase-distribution images

The sum of the elements in M (I_o) represents the intensity of each image, and *P* represents the polarization matrix components. These two inputs were used to identify gases, liquids, and solids in the CO_2 electrolyzer in time and space using the algorithm expressed in Fig. S5. The bulk solid material yields high scattering coefficients, and therefore higher I_o, compared to liquid and gas (Fig. S3). The threshold for assigning the solid phases is I_o > 13 dB. Bulk solids also exhibit a lower differential depolarization index (*DDI* < 0.8) relative to solids and gases (*DDI* > 0.8) (*30*).

The enclosed areas surrounded by the bulk solid phase were then identified as either liquid or gas phase (*31*). Isolated pixels and regions where we are unable to resolve solids, liquids and gases (e.g., solid particles inside gas bubbles) are categorized herein as undefined regions ("U-regions"). Liquid|solid interfaces and gas|solid interfaces also exhibit distinctive Io from those of pure phases of solids, liquids, and gases (*32–34*). Liquids and gases were characterized by I_o values of <7 dB. To resolve the liquids and gases, we compared the slopes of intensity versus depth (slope ratio, SR) at interfaces. Gases were identified if SR < 3, and liquids were identified when SR > 3. U-regions were assigned in cases where SR ≈ 3 *(35–37).*

The pixels in the U-regions were further analyzed with the light polarization matrix data. The polar and differential decompositions were used to resolve gases and liquids. An iterative procedure was applied to ensure the total pixel number (>1k initially) of U-regions was either below 10 for each cross-sectional Z–plane image (>1 million pixels in total), or that the iteration time went beyond 1000 s, in which case a rigid decision based on the other data formed in this task was applied. Thresholding is for initializing the U-regions but is not sensitive to final results.

CO_2 control experiments

To distinguish between CO_2 and other gases in the CO_2 electrolyzer, we first performed a control experiment to identify CO_2. We added 1 M HCl dropwise into a plastic cuvette containing 3 M $KHCO_3$ and a small piece of carbon paper. The carbon paper was added to: (i) provide a nucleation surface similar to the membrane; and (ii) to highlight for the reader how the experiment is able to resolve the bubbles in a vessel containing solid and liquid. CO_2 is the only gaseous product produced upon addition of acid to the $KHCO_3$ solution. We then recorded the optical matrix properties of CO_2, the electrolyte, and the carbon paper in the vessel (Fig. S8, S9). The light polarization matrix data for the experiment was fed into a deep learning model VGG16 (*38*) to yield polarization and intensity data indicating the regions where CO_2 exists. The output polarization and intensity data for the CO_2 regions were similar to that found in literature (Table S1) (*32*–*34*). The entire experiment was repeated 12 times.

This CO_2-detection model was then applied for the entirety of the gas-phase and the U-region data to detect CO_2 regions in the CO_2 electrolyzer (e.g., Fig. S14). We quantified the degree of error for species *i* (Z_i) by comparing the volume of CO_2 detected by eOCT (V_{eOCT}) with the gas volume measured by the mass flow meter (V_m):

$$Z_i = |V_{eOCT} - V_m|/V_m \quad \text{(Eq. S8)}$$

The degree of error in using eOCT for the CO_2 volume determination was 3.4 %.

CO and H_2 identification

The residual gas-phase areas were then identified as CO or H_2 once CO_2 was excluded based on their light polarization properties (Fig. S14). In general, CO has higher DDI but lower anisotropy compared to H_2, and CO_2 has higher DDI and anisotropy than H_2 and CO (*32*). If the data did not

fall into any of the above-mentioned categories, then the corresponding pixels were assigned as the U-region (defined above).

To determine the error in H_2 quantification, we used the eOCT to image the formation of H_2 gas from the reaction between Fe and HCl ($Fe_{(s)} + 2HCl_{(aq)} \rightarrow FeCl_{2(aq)} + H_{2(g)}$). A Fe wire was introduced into the reaction vessel described above containing 1 M HCl. We observed bubbles form by eOCT. We calculated the volume of the H_2 bubbles formed and compared it to the measured flow rate. The degree of error for H_2 was 5.2 %.

S4. Statistical analysis of the chemical species

S4A. Naïve Bayes theorem

In this section, we briefly outline the quantification of the probabilities, degree of error, and concentrations of the chemical species. We used Naïve Bayes to roughly estimate the probabilities of phases for each detected pixel (*39*, *40*). Naïve Bayes is a conditional probability model. Given a problem instance to be classified (in our case, it deals with the classification of the image pixels into 5 different phases: $CO_{2(g)}$, $CO_{(g)}$, $H_{2(g)}$, $H_2O_{(l)}$, and $solid_{(s)}$), represented by a vector $\boldsymbol{X} = [x_1, \ldots, x_n]$, representing *n* independent features for the corresponding instance probabilities:

$$p(C_k \mid x_1, \ldots, x_n) \quad \text{(Eq. S9)}$$

for each of the possible outcomes or classes C_k.

According to Bayes theorem, the conditional probability can be determined as:

$$p(C_k \mid x) = \frac{p(C_k)p(x|C_k)}{p(x)} \quad \text{(Eq. S10)}$$

In practice, only the numerator matters because the denominator does not depend on class *C*. Our features x_i are well-defined, which makes the denominator effectively constant. The numerator is equivalent to the joint probability model $p(C_k, x_1, .., x_n)$, which can be rewritten as follows (*40*):

$$p(C_k \mid x_1, \ldots, x_n) = \frac{1}{Z} p(C_k) \prod_{i=1}^{n} p(x_i \mid C_k) \quad \text{(Eq. S11)}$$

where $Z = p(x) = \Sigma_k p(C_k)p(x \mid C_k)$ is a scaling factor dependent only on $x_1, .., x_n$, that is, a constant if the values of the feature variables are known.

By using the Naïve Bayes conditional independence assumption that all features in *x* are mutually independent and conditional on class C_k., the above equation can be rewritten as (*40*):

$$
\begin{aligned}
p(C_k, x_1, \dots, x_n) &= p(x_1, \dots, x_n, C_k) \\
&= p(x_1 \mid x_2, \dots, x_n, C_k)p(x_2, \dots, x_n, C_k) \\
&= p(x_1 \mid x_2, \dots, x_n, C_k)p(x_2 \mid x_3, \dots, x_n, C_k)p(x_3, \dots, x_n, C_k) \\
&= \cdots \\
&= p(x_1 \mid x_2, \dots, x_n, C_k)p(x_2 \mid x_3, \dots, x_n, C_k) \cdots p(x_{n-1} \mid x_n, C_k)p(x_n \mid C_k)p(C_k)
\end{aligned}
$$

(Eq. S12)

S4B. Method for construction of a classifier from the probability model

The Naïve Bayes classifier usually combines the Naïve Bayes probability model with a decision rule (*40*). One common rule is to pick the hypothesis that is most probable so as to minimize the probability of misclassification, which is also known as the maximum a posteriori probability (MAP) decision rule. The corresponding classifier, a Bayes classifier, is the function that assigns a class label $\hat{y} = C_k$ *a*s follows (*40*):

$$\hat{y} = \underset{k \in \{1,\dots,K\}}{\operatorname{argmax}} p(C_k) \prod_{i=1}^{n} p(x_i \mid C_k) \qquad \text{(Eq. S13)}$$

In this eOCT study, we defined K= 5, which represents the 5 component phases of an image pixel where C_1 for solid$_{(s)}$, C_2 for electrolyte$_{(l)}$, C_3 for $CO_{2(g)}$, C_4 for $CO_{(g)}$, and C_5 for $H_{2(g)}$. Parameters x_1, x_2, and x_3 indicate the anisotropy, scattering intensity, and DDI, respectively. The distribution of feature x_1 (anisotropy) is shown in Fig. S14 as an example.

<u>Quantification of the degree of error with statistical analysis of large data sets</u>

The Bayes theorem can be used to quantify the probabilities for each phase on a single pixel basis given a sufficient amount of data (usually > 100 GB). Here we quantified the Bayes classification accuracy of solid$_{(s)}$, liquid$_{(l)}$, $CO_{2(g)}$, $CO_{(g)}$, and $H_{2(g)}$ based on the 100 sets of available data (> 10 TB). For each segmented phase component, the Bayes classification accuracy (*p)* of each phase was calculated to be p_{solid} = 0.93, $p_{electrolyte}$ = 0.83, $p_{CO2(gas)}$ = 0.91, $p_{co(gas)}$ = 0.88, and $p_{H2(gas)}$ = 0.84, respectively.

S4C. Multiple phase statistical analysis

We have shown in the main text the distribution of $CO_{2(g)}$, $H_{2(g)}$, and $CO_{(g)}$ (chemical maps) inside the electrolyzer (Fig. 4). The goal of this section is to determine the precision and accuracy of the eOCT measurements, as well as to discuss the phenomenon of phase mixing and transporting that relates to the reactions.

The concentrations of gases

The observation of $CO_{2(g)}$, $CO_{(g)}$, and $H_{2(g)}$ in our experiment indicated that the concentrations of dissolved $CO_{2(aq)}$, $CO_{(aq)}$, and $H_{2(aq)}$ in the cathode chamber reach their solubility limit. The volume fraction of each gas (f_i) was calculated using $f_i = V_i/(V_{CO2}+V_{H2}+V_{CO})$, where V_i is the volume of each gas component ($CO_{2(g)}$, $CO_{(g)}$, or $H_{2(g)}$). The volume of each gas was quantified by calculating the total pixels of each gas in the 3D volumetric data $V_{(x,y,z)}$. The mole amount of each gas can be calculated using the ideal gas law $PV = nRT$ at ambient conditions based on the volumetric data.

The probability maps

In order to track the conversion of $CO_{2(g)}$ to $CO_{(g)}$, the occurrence of each phase must be unambiguously defined and located in both space and time. One can easily yield the probability of spatial distributions for $CO_{2(g)}$, $CO_{(g)}$, $H_{2(g)}$, $H_2O_{(l)}$, and $solid_{(s)}$ by applying statistical analysis (methods in Section S4A, B) on all the images obtained. The 2D probability maps of different phases i.e., $CO_{2(g)}$, $CO_{(g)}$, $H_{2(g)}$, $H_2O_{(l)}$, and $solid_{(s)}$ in the X–Z plane of the electrolyzer are obtained with examples of the three gas phases shown in Fig. S15. We define the probability of TPCs (origination) as the joint probability of reactants; i.e., $electrolyte_{(l)}$, $CO_{2(g)}$, and $solid\ catalyst_{(s)}$ (Renyi's axiom of probability (*42*)). We define the probability of $CO_{(g)}$ generation (Eq. S11, Fig. S19A) as the Gaussian probability distribution of $CO_{(g)}$ in an eOCT image based on various light properties (i.e., intensity, anisotropy, and DDI) (*43*). We applied different time shifts (Δt) to

traverse the possible time sequence arrangement between the originating and generation probability.

Our analysis revealed a large spatial overlap of > 95% (Fig. S19B) and a strong dependence (Fig. S19C) between $CO_{(g)}$ generation (d_{CO}/dt) and the TPC origination probability. This quantification supports our qualitative findings in Fig. S18. The time delay between $CO_{(g)}$ generation and the TPC origination probability is close to zero (< 1 ms) (Fig. S19C, right). These observations show that $CO_{(g)}$ generation occurs immediately after the TPC origination probability reaches 0.01%. The current results agree with recent theory and experiments which show that TPCs play a critical role in CO2RR (*44*, *45*). The probability of the bulk existence (*46*) of a phase (i.e. $CO_{2(g)}$, $CO_{(g)}$, or $H_{2(g)}$) is distributed according to Beta function whereas the sharp Gaussian peak corresponds to the probability distribution of the transient generation of a phase (Fig. S19A). The spatial map for $CO_{2(g)}$ origination highly overlaps with its generation map (> 99 %) (Fig. S19B), which confirms the $CO_{2(aq)} \rightleftarrows CO_{2(g)}$ equilibrium.

Phase mixtures

$CO_{2(g)}$, $CO_{(g)}$ and $H_{2(g)}$ coexist in different proportions in the gas bubbles generated at the cathode surface. Phase mixtures can be observed in our 2D probability maps (Fig. S15) of $CO_{2(g)}$, $CO_{(g)}$, $H_{2(g)}$, $H_2O_{(l)}$, and $solid_{(s)}$. The phase mixing can be attributed to mass transport effects (e.g. convective mixing caused by bubble growth or collapse), chemical reactions, and the super-positioning of phases at spatial- or temporal-scales below the detection limit of eOCT. The probability of each chemical species (Fig. S15) for a single pixel in the 2D map is calculated by the Naïve Bayes theorem as described in Section S4A and 4B.

S5. Supporting figures

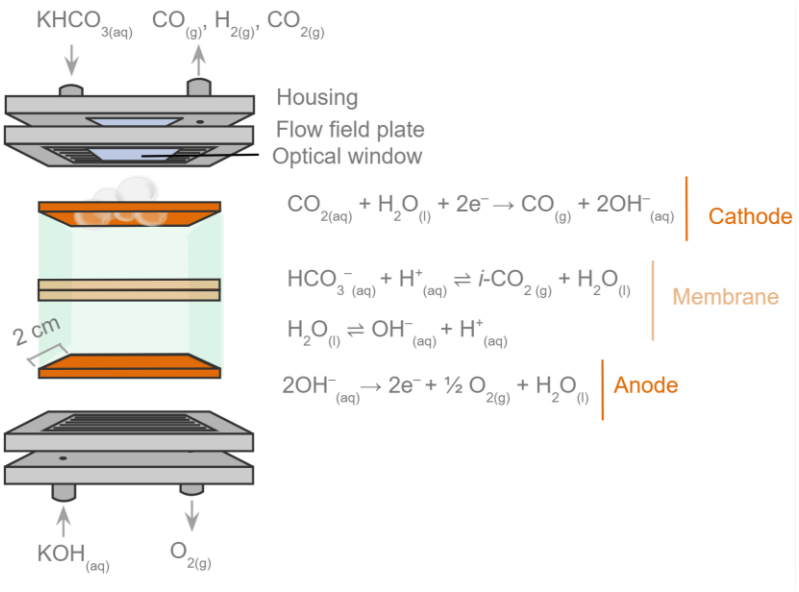

Fig. S1. Expanded view of the CO_2 electrolyzer used for this study. We applied a current of 100 mA cm^{-2} to produce CO from a $KHCO_3$ solution. A bipolar membrane (BPM) is between the nickel foam anode and gas diffusion cathode. 1 M KOH and 3 M $KHCO_3$ solutions were fed to the anode and cathode compartments, respectively.

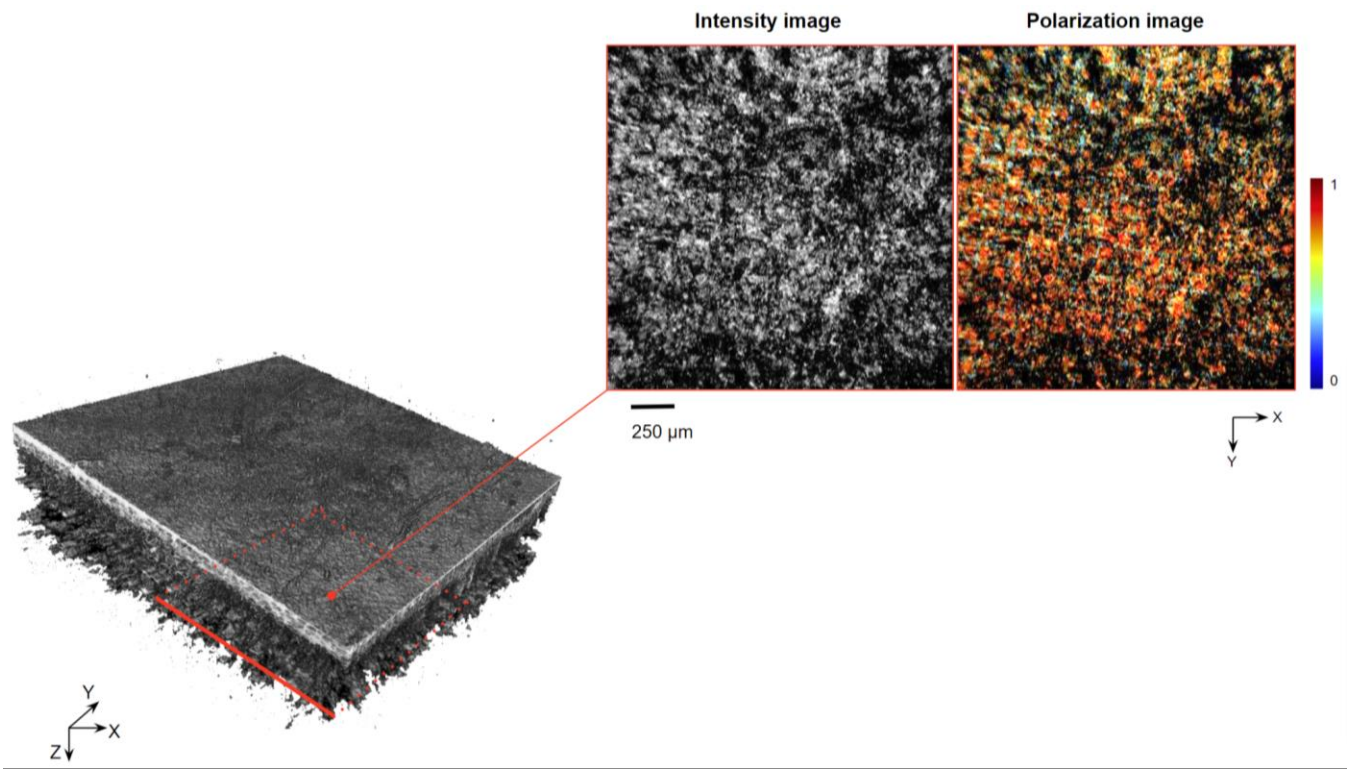

Fig. S2. Electrolysis optical coherence tomography (eOCT) intensity (gray-scale) and polarization (coloured) images of the surface of the Ni foam anode (X–Y plane). The red line on the 3D image represents the depth (Z–plane) at which the image was captured in the CO_2 electrolyzer and the dotted red line represents the location of the entire 2D polarization and intensity images. Blue represents low degree of polarization (DOP) and red represents high DOP.

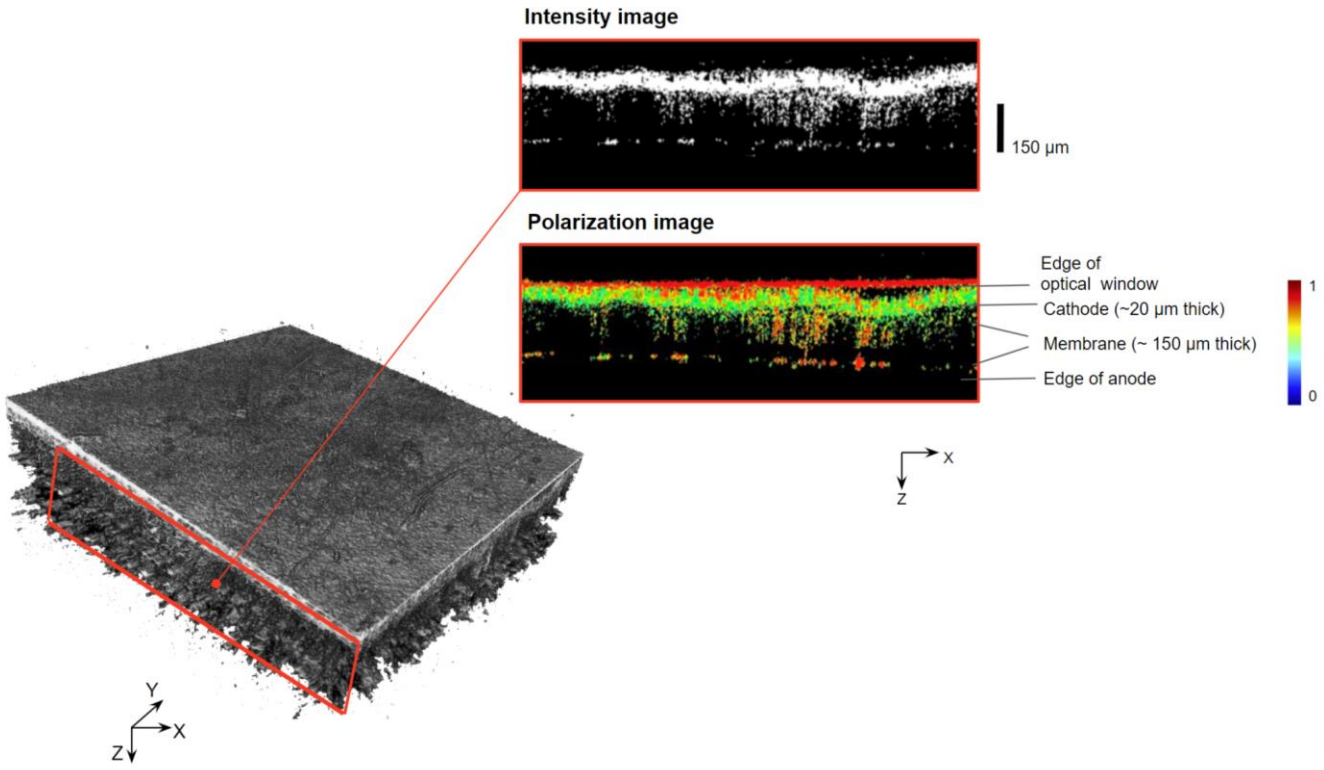

Fig. S3. Electrolysis optical coherence tomography (eOCT) intensity (gray-scale) and polarization (coloured) images of the cross-section (X–Z plane) of the CO_2 electrolyzer. Red represents high DOP value (>0.7) and green represents DOP of ~0.5 in the polarization image.

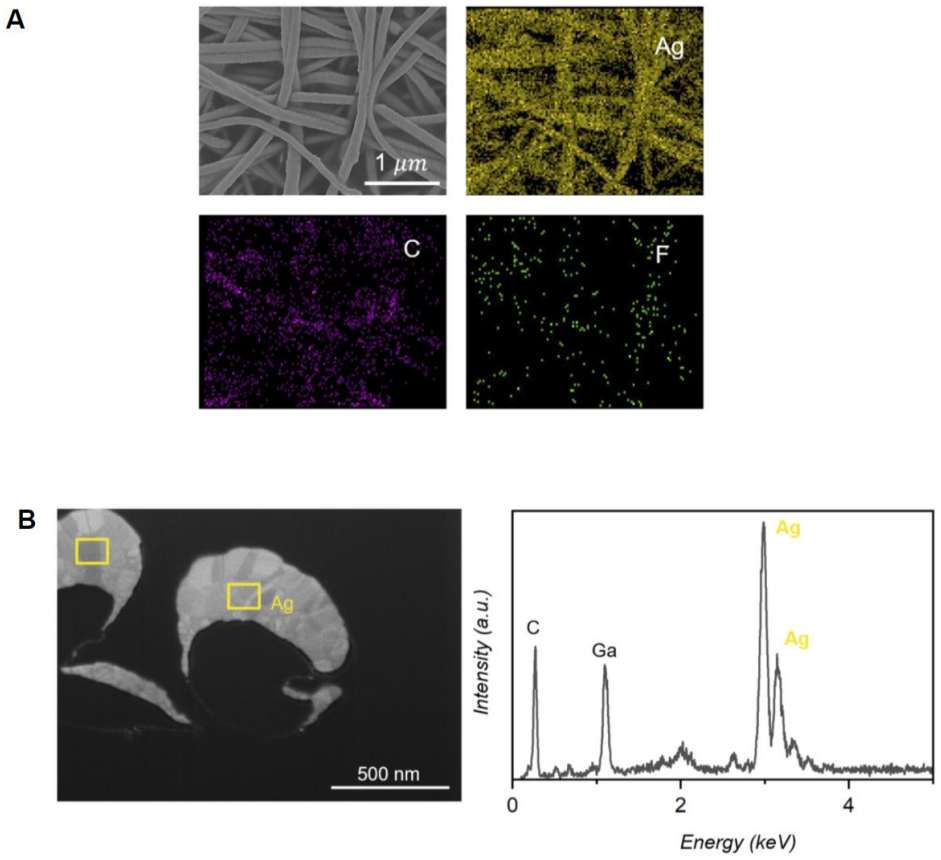

Fig. S4. (**A**) Scanning electron microscope (SEM) image of a Ag-sputtered electrospun gas diffusion cathode, and the corresponding elemental map for Ag (yellow), C (purple), and F (green) obtained from energy-dispersive X-ray (EDX) spectroscopy. The elemental map shows that Ag is evenly distributed across the surface of the nanofibers. (**B**) A cross-section SEM image of the cathode reveals a tubular Ag electrocatalyst shell on the surface of a nanofiber, confirmed with EDX spectroscopy.

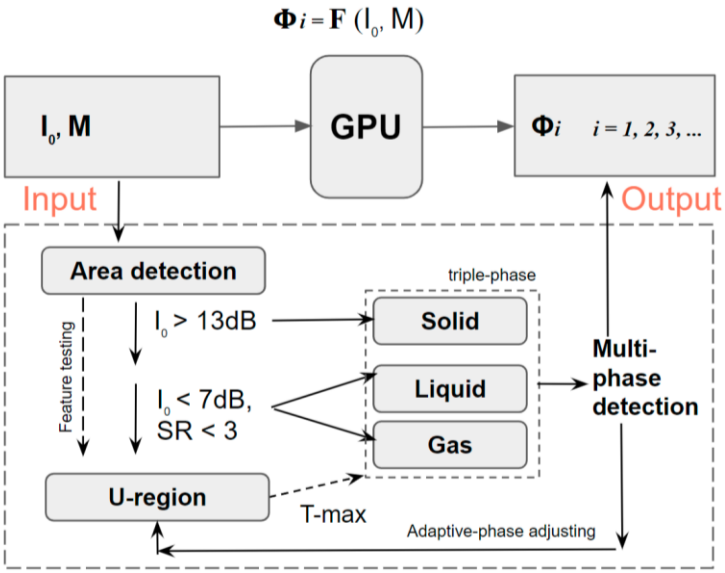

Fig. S5. Decision matrix used to produce phase-distribution images, where *M* represents 16 polarization matrix components, and I_0 is the intensity of each image. The multiphase (Φ) is a function (F) of intensity and polarization. Gas, liquid, and solid phases were determined by characterizing the co-registered signals of each pixel or enclosed area in all polarization images and related features (e.g., DDI).

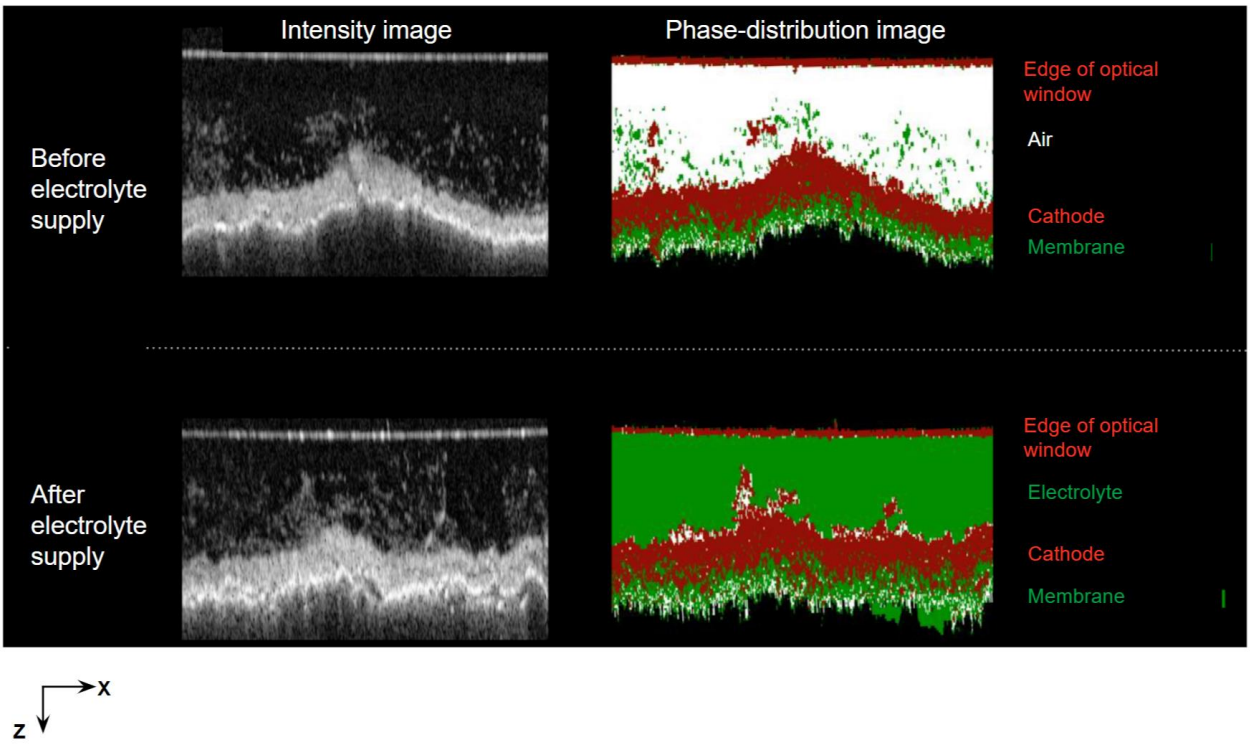

Fig. S6. Intensity and phase–distribution images captured by the electrolysis optical coherence tomography platform before (top) and after (bottom) electrolyte is supplied to the CO_2 electrolyzer. Both images show a cross-section (X–Z plane) of the electrolyzer. Intensity images show a grayscale of the light intensity properties (white being lower intensity, black being higher intensity). Phase–distribution images show solid-phase (red), liquid-phase (green), and gas-phase (white) obtained using the decision matrix shown in Figure S5.

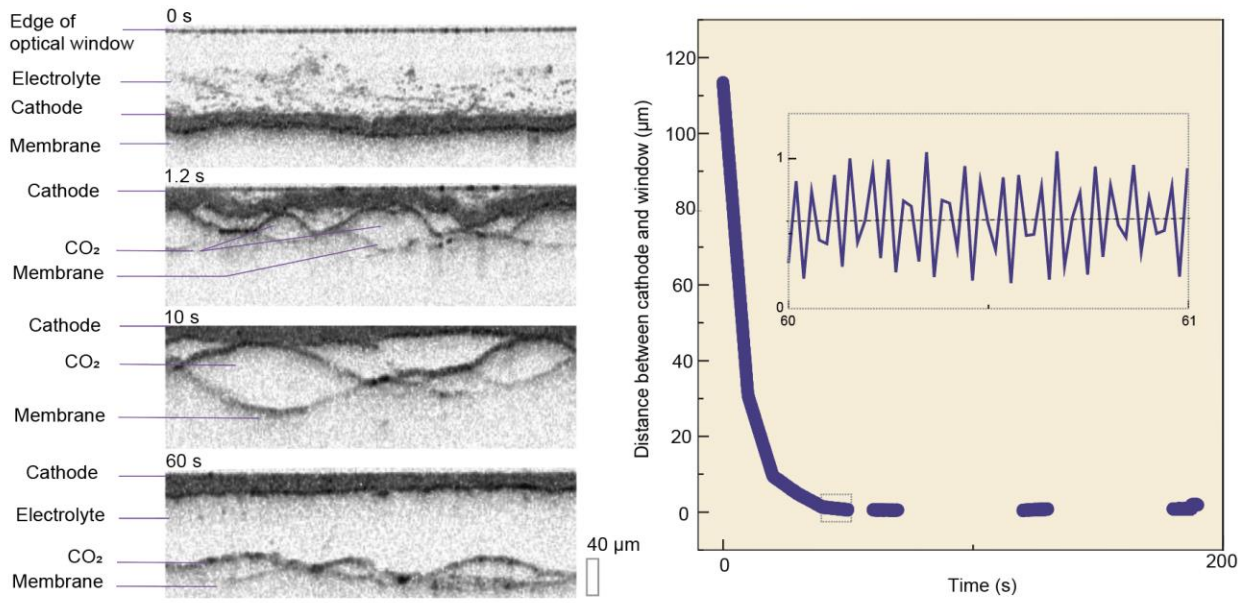

Fig. S7. Intensity images at 0–60 s after 100 mA cm^{-2} was applied to the CO_2 electrolyzer. At 0 s, electrolyte is flowing through the electrolyzer. At 1–60 s of galvanostatic electrolysis, the distance between the cathode and optical window steadily decreases. After 60 s, the cathode oscillated between being in contact with the optical window and the membrane.

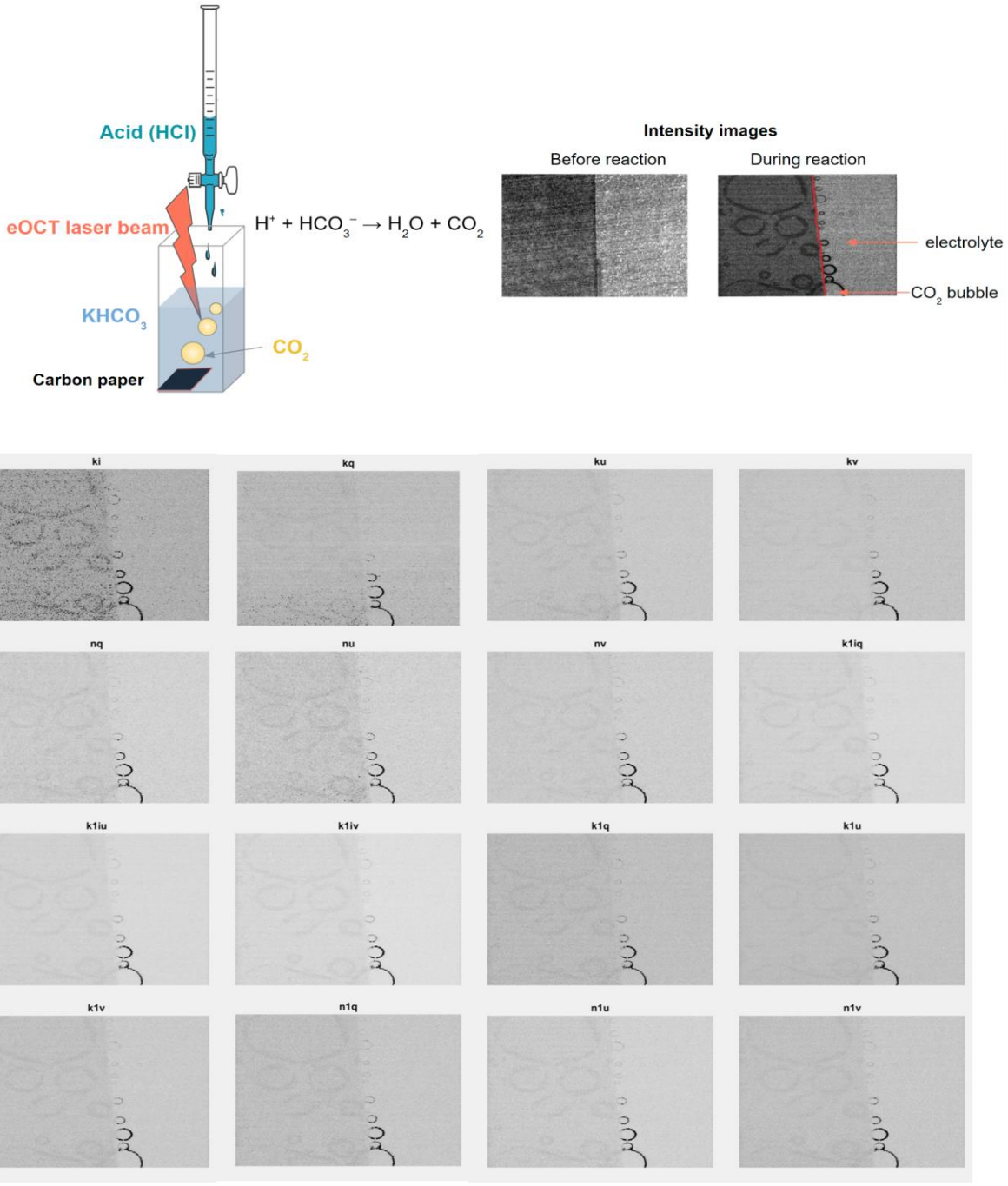

Fig. S8. Optical coherence tomography polarization images of a control experiment where CO_2 bubbles are produced in a transparent tube containing carbon paper in a mixture of 1 M HCl and 3 M $KHCO_3$. The carbon paper is intended to mimic the surface of the membrane. The light properties of these CO_2 bubbles were used to identify the CO_2 bubble in the CO_2 electrolyzer produced during electrolysis. The 16 polarization images represent the 16 light property components of Equation S6.

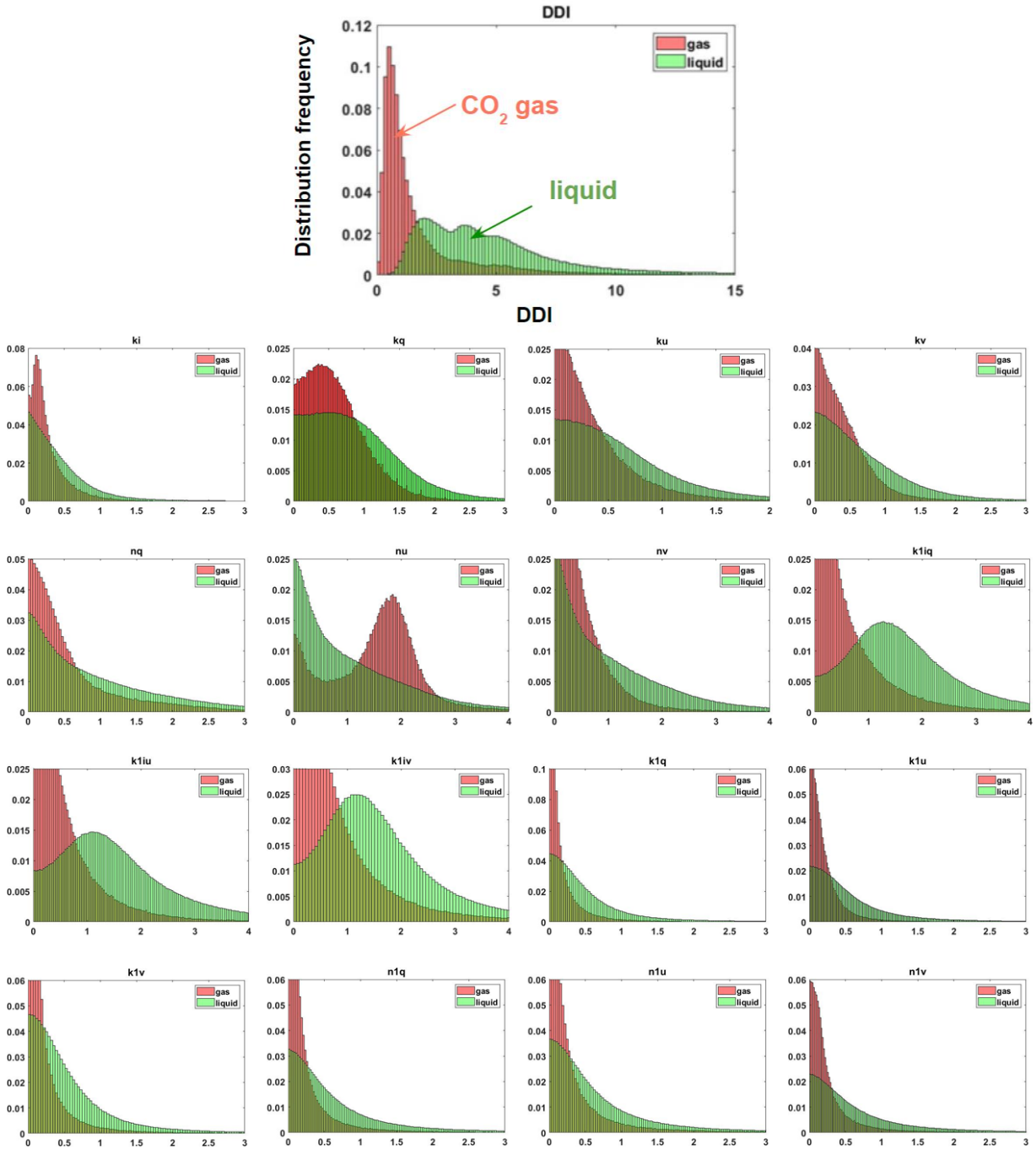

Fig. S9. Differential depolarization index (DDI) distribution frequency of CO_2 and electrolyte obtained from the same control experiment in Figure S8, where we produced CO_2 bubbles in a transparent tube from a mixture of 1 M HCl and 3 M $KHCO_3$. The DDI of CO_2 is distinctive from the DDI of the electrolyte. The 16 plots represent the 16 light property components of Equation S6.

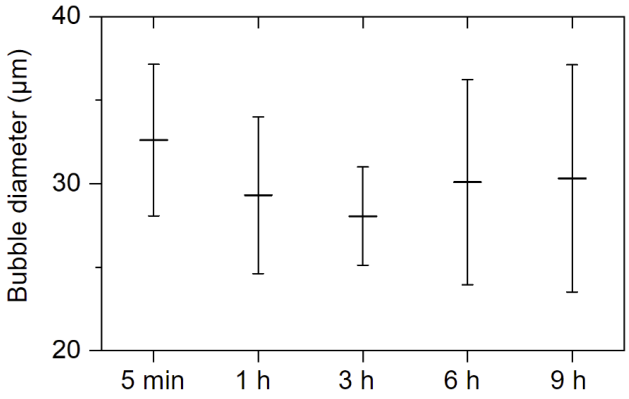

Fig. S10. Average bubble diameter captured in snapshots taken at 5 min, 1 h, 3 h, 6 h, and 9 h of electrolysis. The bubbles grow to an average size of ~30 µm during electrolysis. Error bars represent the standard deviation determined from the quantification of bubbles in a 1 mm by 100 µm window.

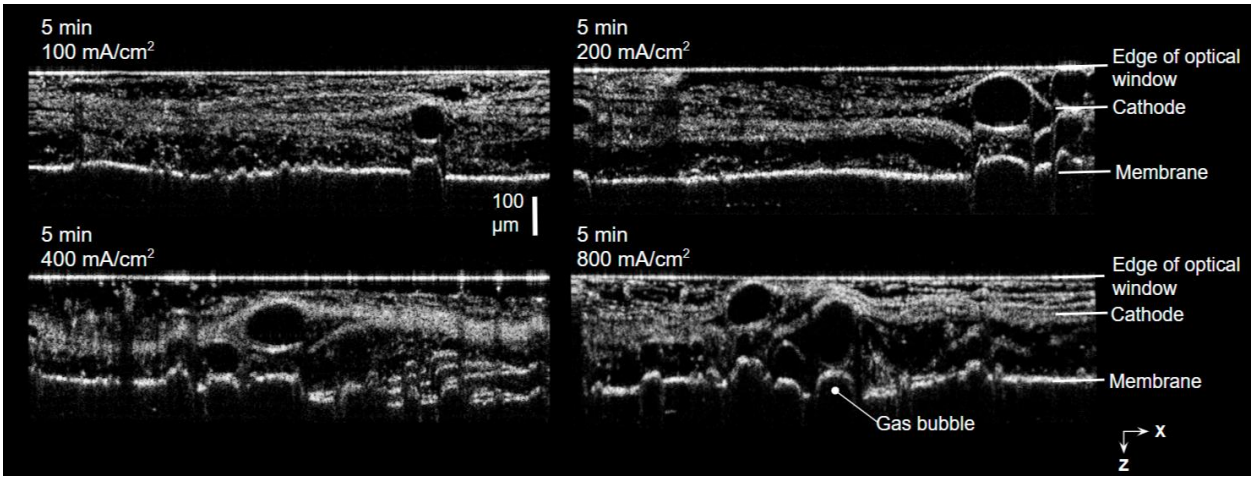

Fig. S11. Intensity images of the X–Z plane (cross-section) of a CO_2 electrolyzer captured by eOCT at 5 min under current densities of 100–800 mA cm^{-2}.

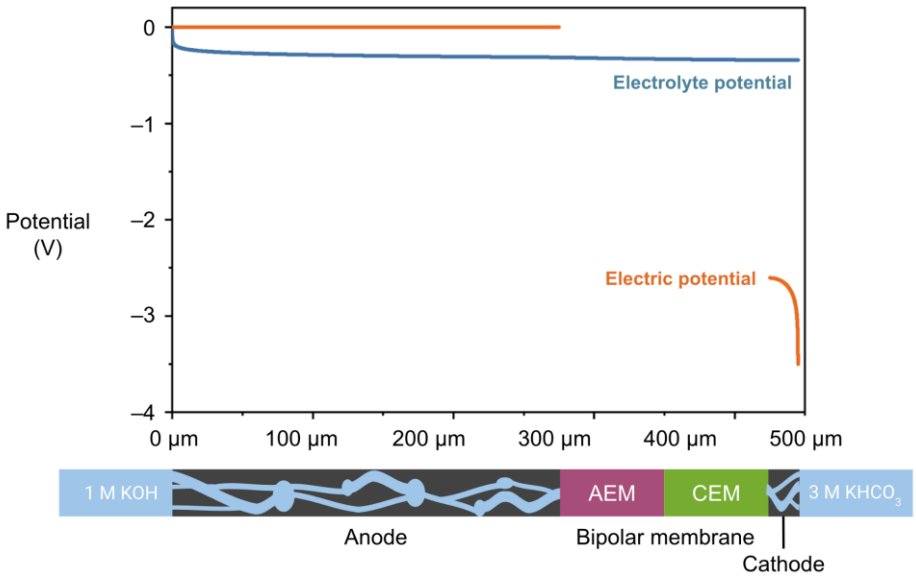

Fig. S12. Modeled potential profiles from the 1D continuum model of the eOCT.

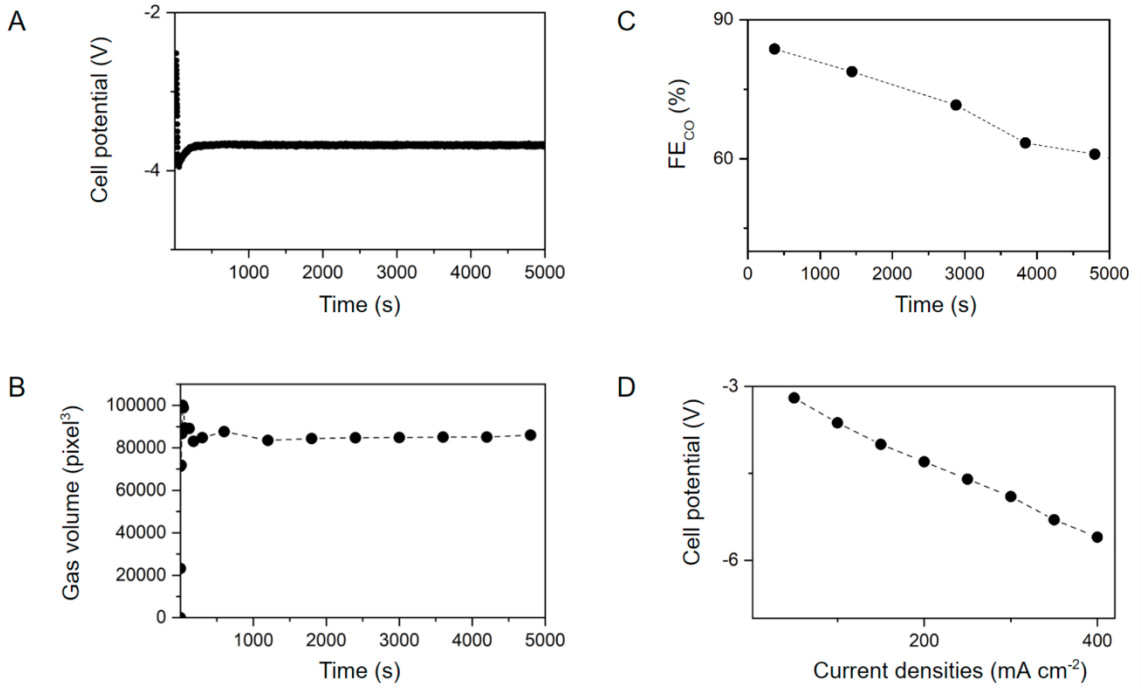

Fig. S13. (A) Cell voltage with corresponding **(B)** gas volume, **(C)** faradaic efficiency of CO (FE_{CO}) measured as a function of time at a constant current density of 100 mA cm^{-2} and **(D)** cell potential in response to the applied current densities for CO2RR electrolysis.

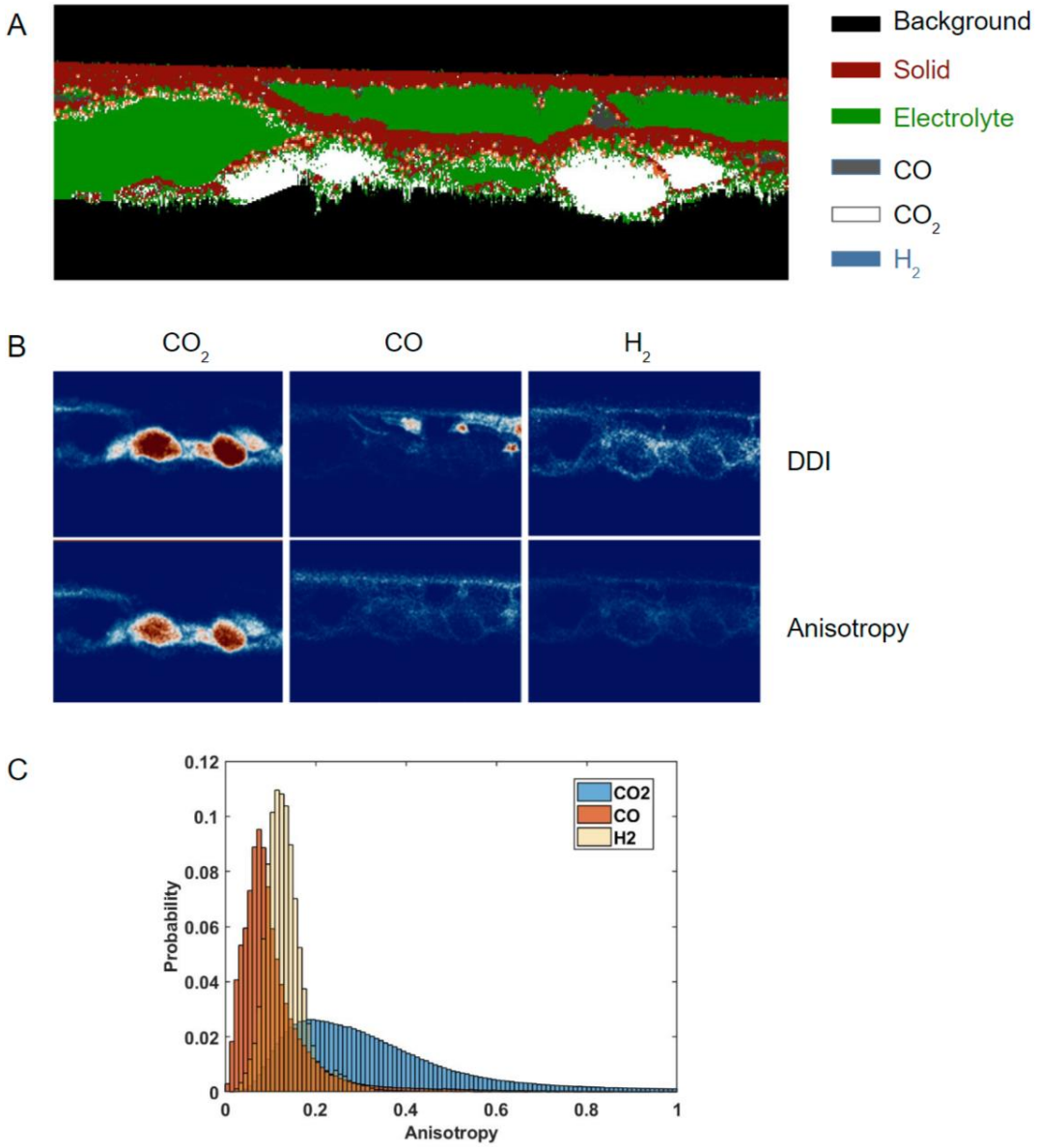

Fig. S14. **(A)** Phase-distribution image of the X–Z plane at t = 5 min from Figure 3 showing solids (i.e., catalyst and membrane), electrolyte, CO, CO_2 and H_2. **(B)** Parameters of differential depolarization index (DDI) and anisotropy for CO_2, CO, and H_2 bubbles, respectively corresponding to the same location as the phase-distribution image. DDI was calculated according to Equation S7. **(C)** Histogram (normalized probability distribution) of anisotropy for CO_2, CO and H_2.

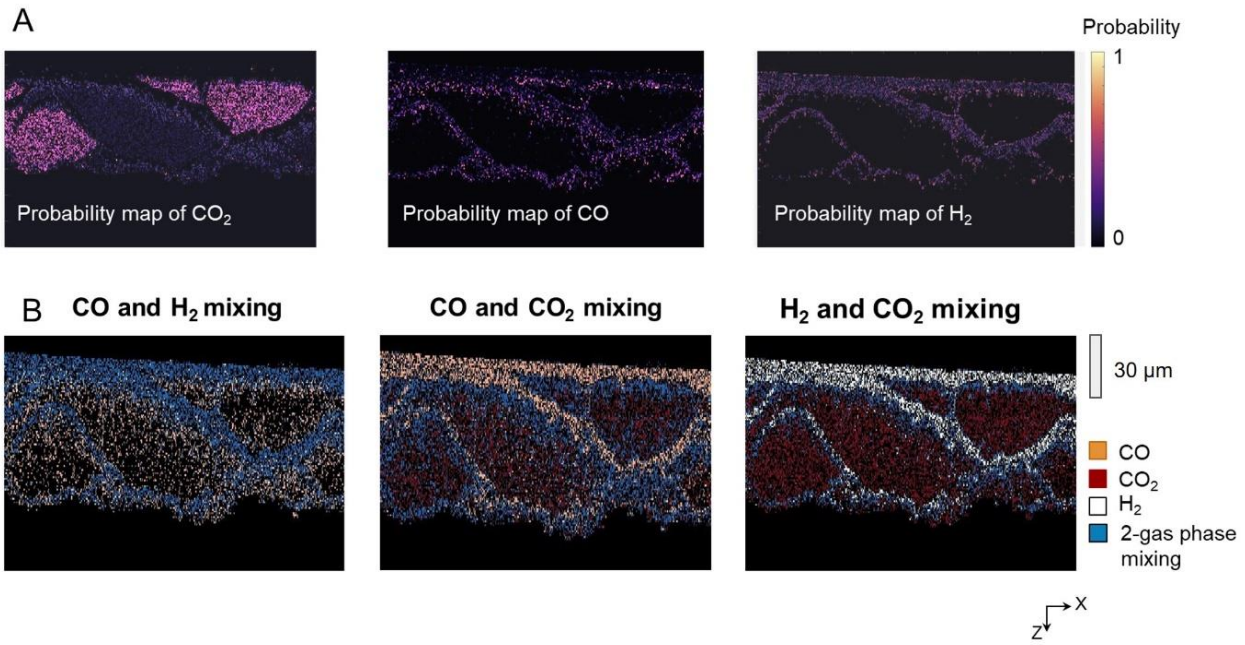

Fig. S15. **(A)** Probability maps of $CO_{2(g)}$, $CO_{(g)}$, and $H_{2(g)}$ in the eOCT under an applied current of 100 mA cm^{-2}. Colours represent the probability of each gas with white representing 1 and black representing 0 (see colour bar). **(B)** The distributions of $CO_{2(g)}$, $CO_{(g)}$, $H_{2(g)}$ and mixtures of gases for data shown in (A). $CO_{2(g)}$ is highlighted in red, $CO_{(g)}$ in orange, and $H_{2(g)}$ in white. The phase mixtures are highlighted as blue.

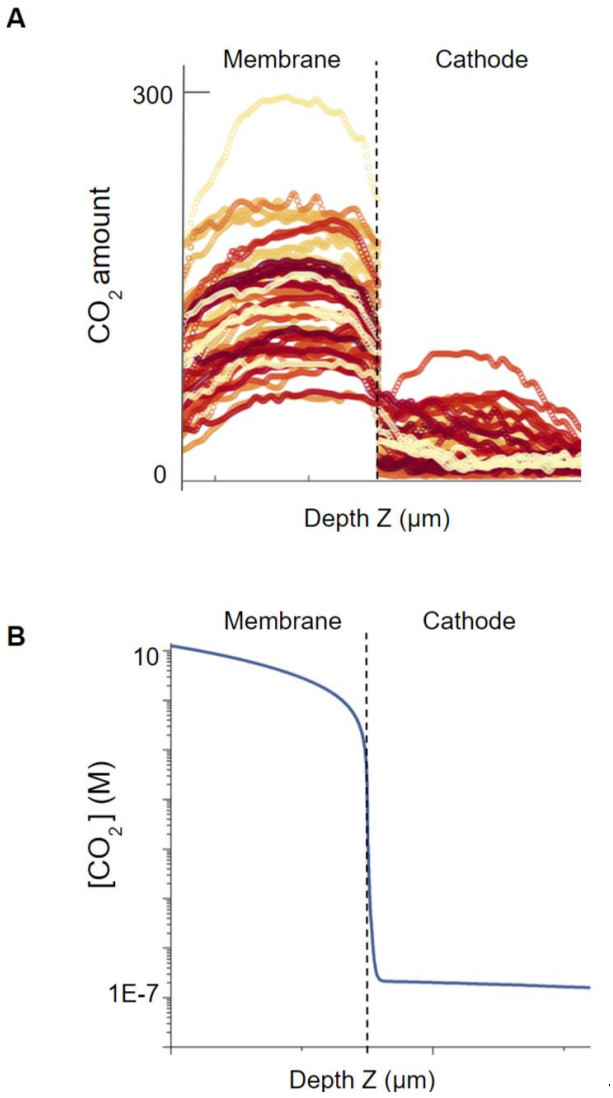

Fig. S16. Experimental and model of CO_2 signals measured by electrolysis optical coherence tomography (eOCT). **(A)** CO_2 signals captured by eOCT were integrated in 3 dimensions over a 0.3-s time frame to yield the amount of CO_2 (i.e., molar counts) and plotted against the depth profile (i.e., vertically in the Z plane starting at the top of the cathode. **(B)** Model of the CO_2 concentration in a CO_2 electrolyzer at a current density of 100 mA cm^{-2} as per work by Lees et. al (*46*). The continuum model solves mass, charge, and momentum transport equations in a 1D porous domain to define the CO_2 concentration profile. The model and experimental data both show a steep CO_2 concentration gradient at the membrane|cathode interface.

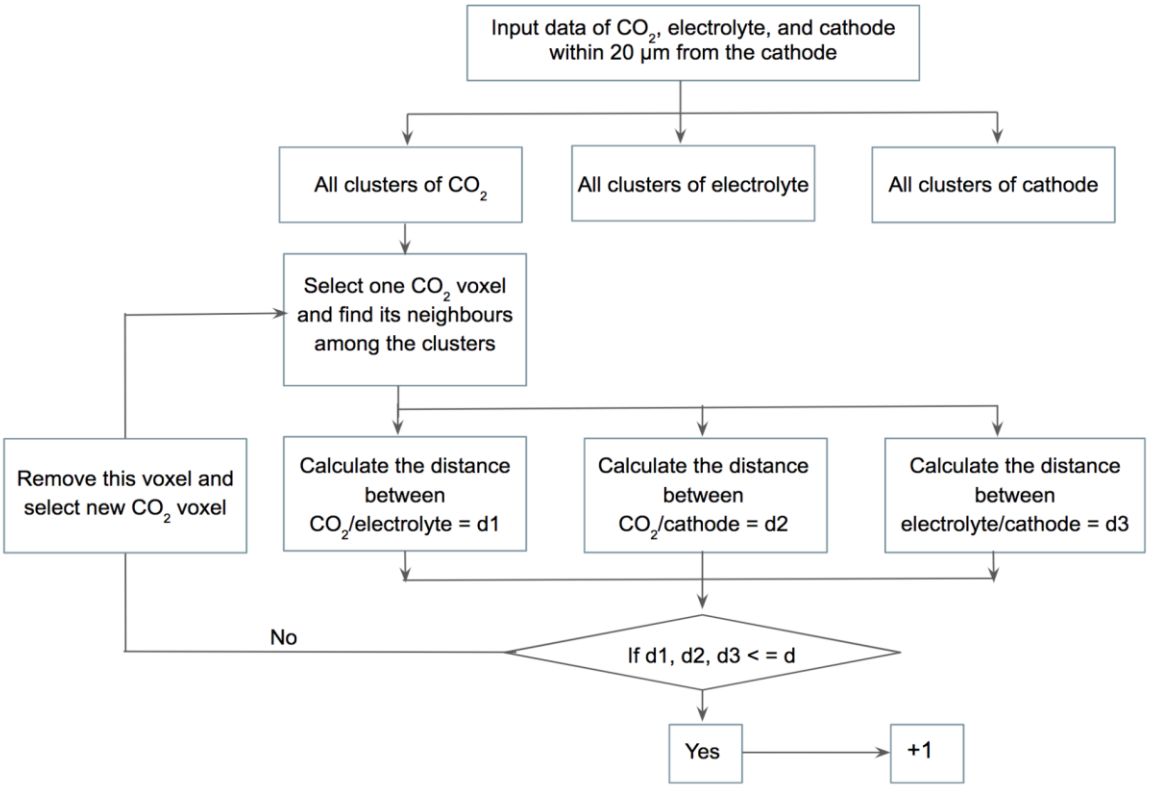

Fig. S17. Decision matrix used to identify triple-phase contacts, in accordance with literature procedures (*48*, *49*).

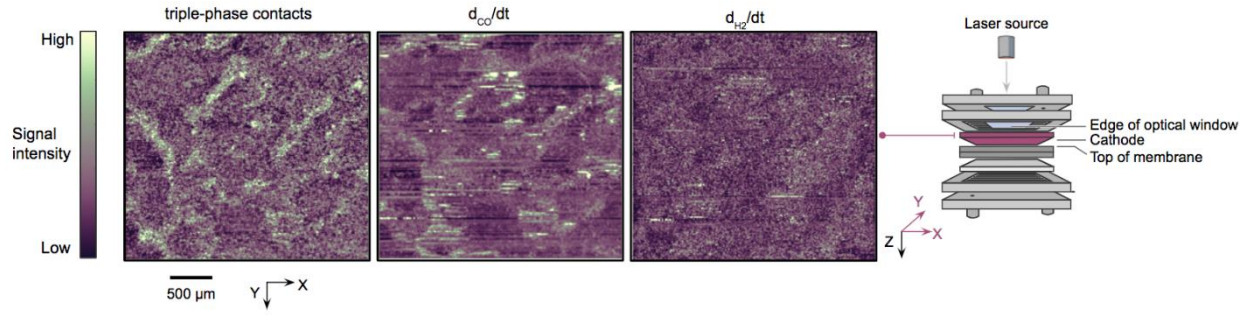

Fig. S18. Phase-distribution images showing the relationship between CO and H_2 formation rates and triple-phase contacts. The images captured by electrolysis optical coherence tomography (eOCT) illuminate triple-phase contacts (i.e., regions where CO_2 gas is in contact with liquid electrolyte and solid cathode), the changes in the amounts of CO (d_{CO}/dt) and H_2 (d_{H2}/dt) over time. The eOCT projections of the cathode were rendered using 200 slices of the X–Y plane over a depth range of 200 μm starting from the edge of the optical window to the top of the membrane. The images were taken between 7.5 and 7.6 min of electrolysis.

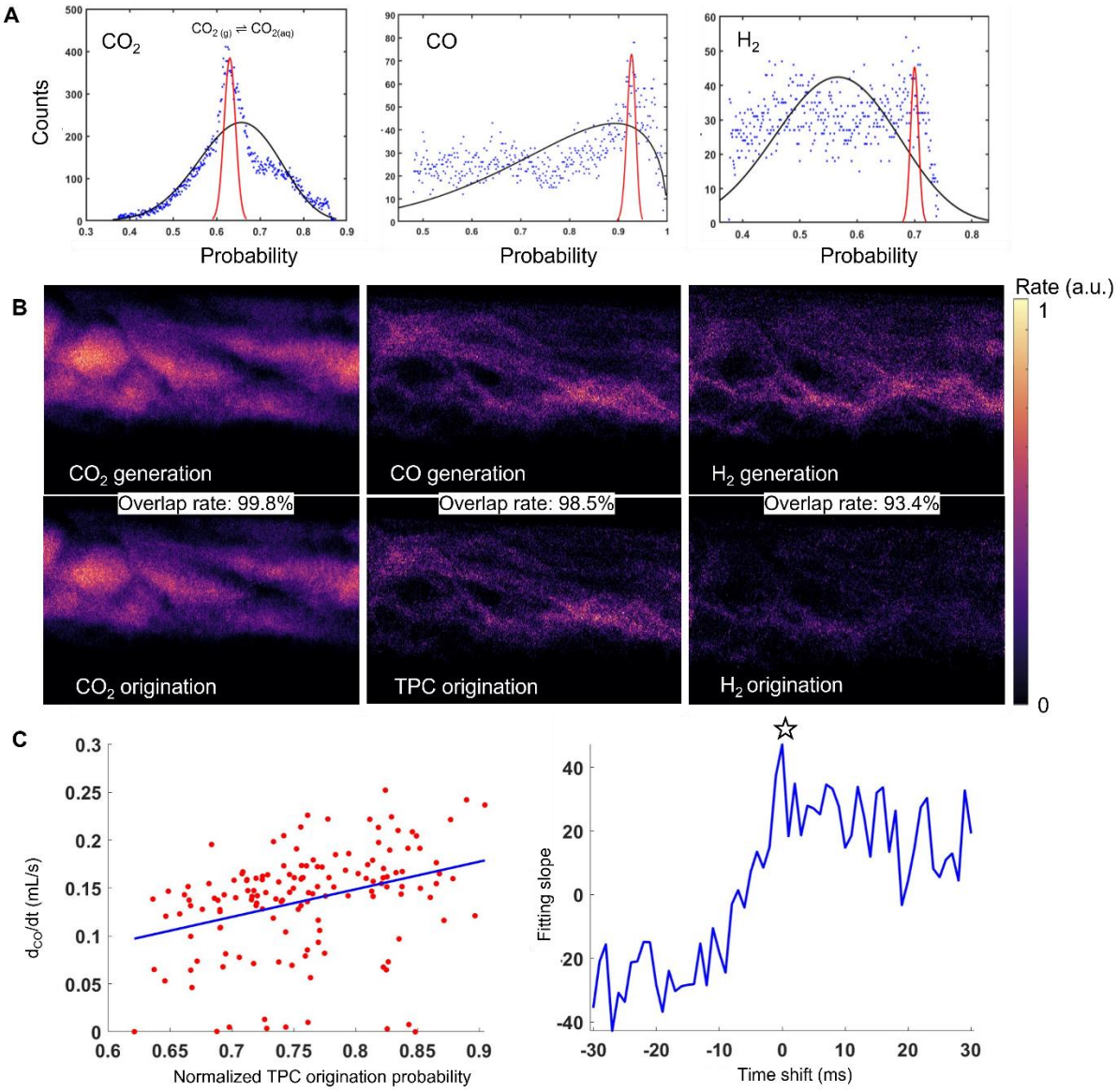

Fig. S19. (**A**) The probability distribution of $CO_{2(g)}$, $CO_{(g)}$, and $H_{2(g)}$ in a region of the eOCT image. Each probability distribution can be readily decomposed into Gaussian and Beta functions. The red Gaussian fitting curve represents the probability distribution of transient generation of $CO_{2(g)}$, $CO_{(g)}$, or $H_{2(g)}$. The black Beta functions represent the bulk existence of $CO_{2(g)}$, $CO_{(g)}$, or $H_{2(g)}$. (**B**) The spatial maps (generated by eOCT) showing the respective generation and origination overlap for different gases. (**C**) Left: Correlation between $CO_{(g)}$ generation (d_{CO}/dt) and the TPC origination probability, quantified by linear regression (*50*). The phase-distribution images that correspond to the data are shown in Fig. S18. Right: time shifts applied to the left profile for quantifying correlation (fitting slope) between $CO_{(g)}$ generation and the TPC origination probability. The time delay between $CO_{(g)}$ generation and TPC origination is close to zero (marked by a star).

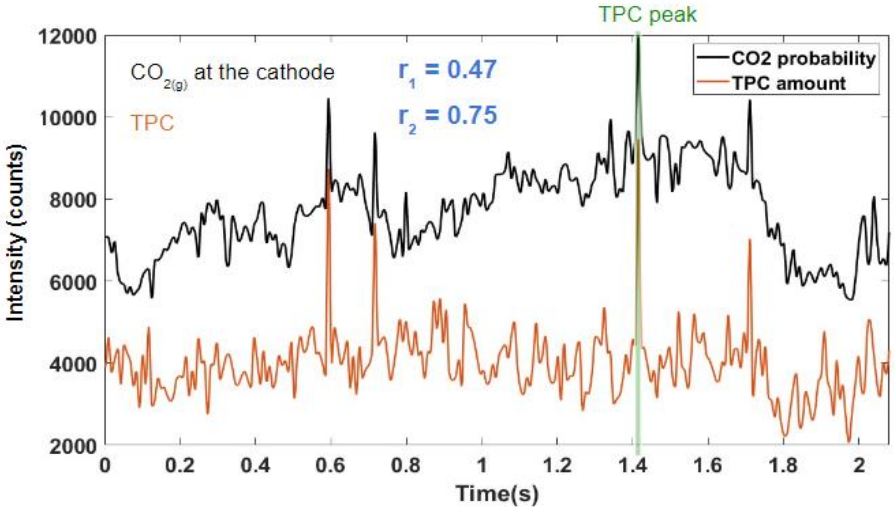

Fig. S20. Counts of $CO_{2(g)}$ and triple-phase contacts (TPCs) at the cathode as a function of time. The peaks in the TPC profile coincide with that of $CO_{2(g)}$. The method and accuracy of $CO_{2(g)}$ detection at the cathode surface by electrolysis optical coherence tomography (eOCT) are described in Sections S3 and S4. The decision matrix used to identify TPCs is shown in Figure S17. Here, r_1 is the correlation coefficient between the black and orange curves; r_2 is the correlation coefficient between the peaks of both curves; this correlation is equivalent to the posterior probability of TPCs (Eq. S11), proving that $CO_{2(g)}$ is the critical source of TPC recovery in the peaks.

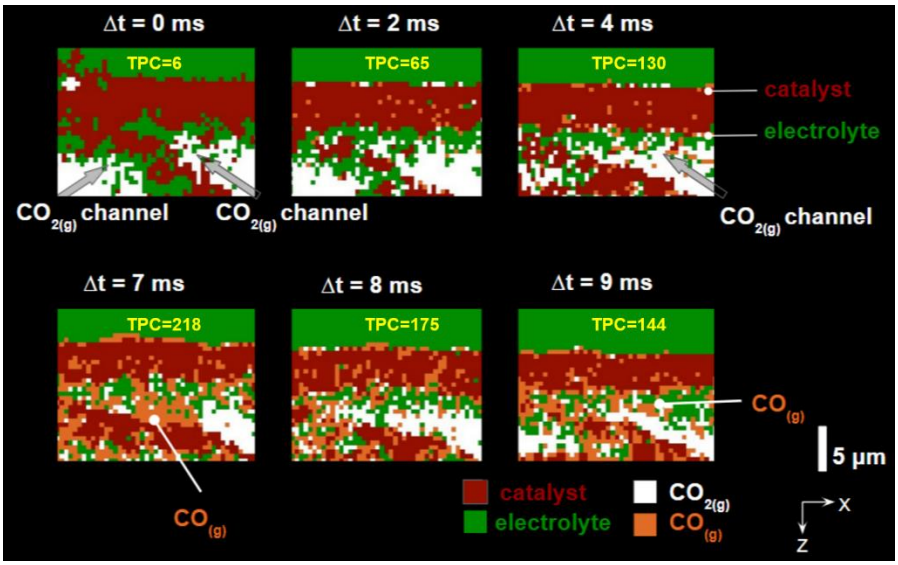

Fig. S21. Phase distribution images of the X–Z plane showing the existence of $CO_{2(g)}$ channels (white) extending at the catalyst (red) to generate $CO_{(g)}$ (orange). Phase–distribution images, obtained from the spatially and temporally resolved data extracted from the TPC peak marked in Fig. S20, shows solid catalyst-phase (red), liquid electrolyte-phase (green), and gas $CO_{2(g)}$-phase (white) obtained using the decision matrix shown in Fig. S5. The method and accuracy of phase detection are described in Sections S3 and S4. A corresponding movie is provided (Movie S7).

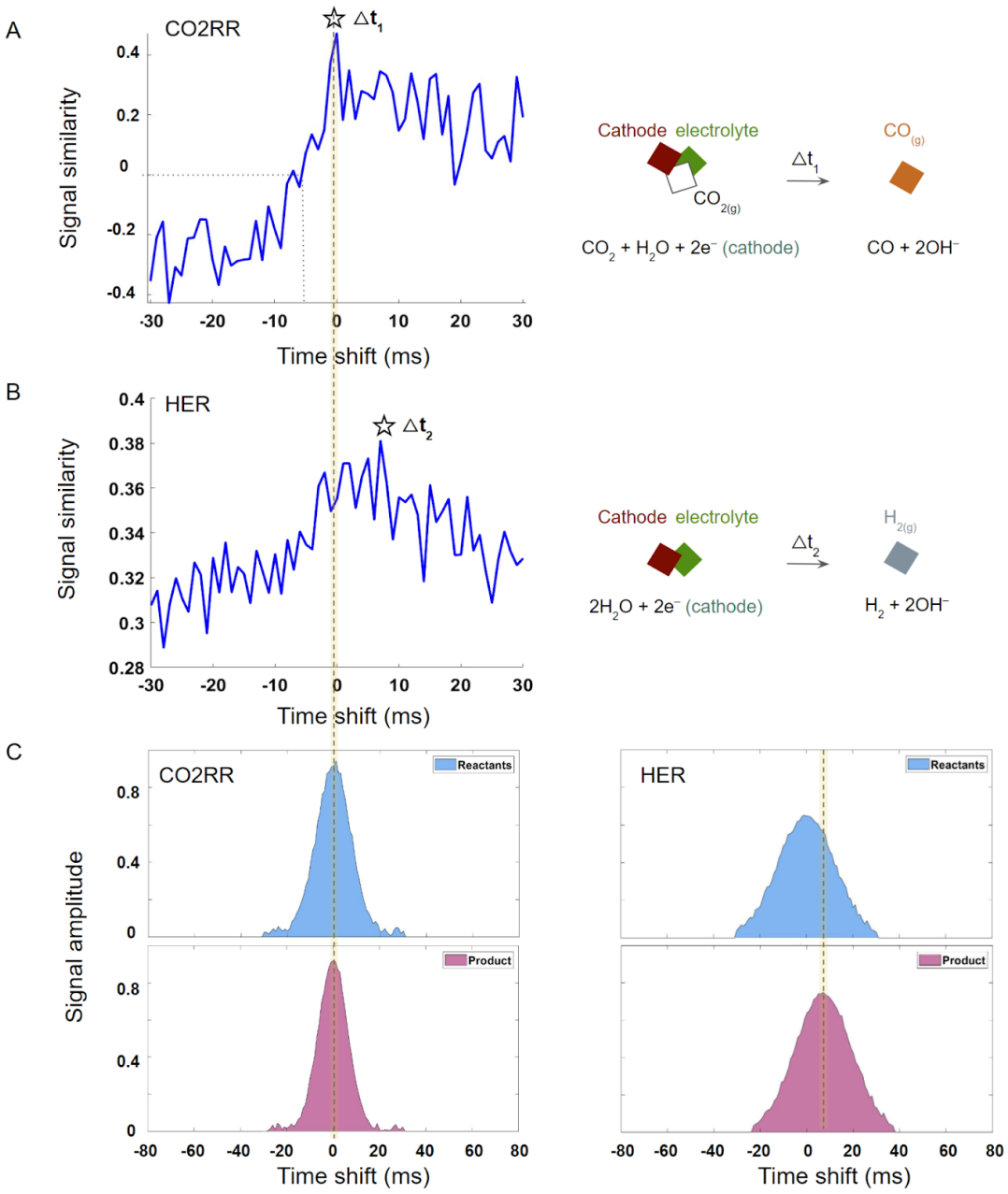

Fig. S22. **On the Ag catalyst surface, CO2RR occurs almost instantaneously, while HER is delayed.** (A) The signal similarity between $CO_{(g)}$ generation and the TPC origination probability with respect to time. The time delay between $CO_{(g)}$ generation and TPC origination is close to zero (Δt_1) (Fig. S19). (B) The signal similarity between H_2 product generation and the probability of H_2 origination (reactants) at the electrolyte|cathode with respect to time. The peak represents a ~7 millisecond delay (Δt_2) between H_2 origination and generation. The demonstration of signal similarity between reactants and products is depicted in Movie S8. Note that the signal similarity goes below 0 at a certain time shift happening before the peak in (A), implying that the residual CO accumulation suppresses the CO2RR within a few milliseconds, which is in line with the time shift (Δt_2) in (B) and the time of CO blockage in Fig. S21.

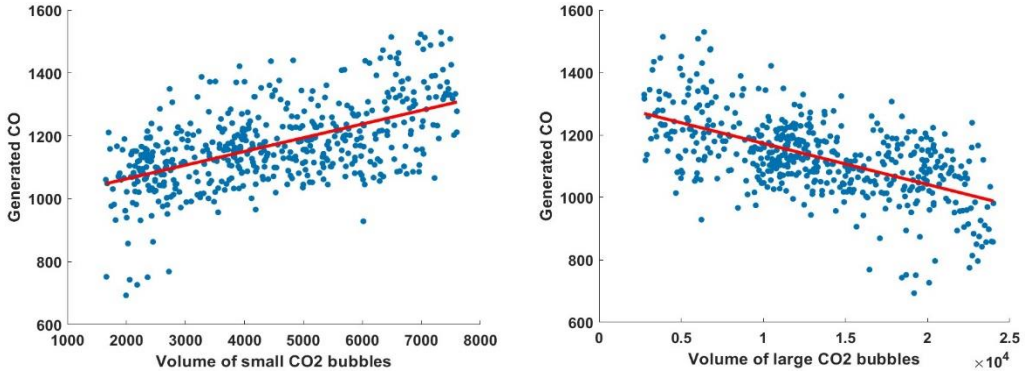

Fig. S23. **Correlation between CO_2 bubble size and CO generation at the cathode**. Small and large CO_2 bubbles were distinguished by a simple threshold that small CO_2 bubbles take up a volume of <1000 μm^3, while large CO_2 bubbles take up a volume of >1000 μm^3. We fitted the scatter points using linear regression (*50*). We observed that small CO_2 bubbles are more likely to promote CO generation, while large CO_2 bubbles suppress CO2RR.

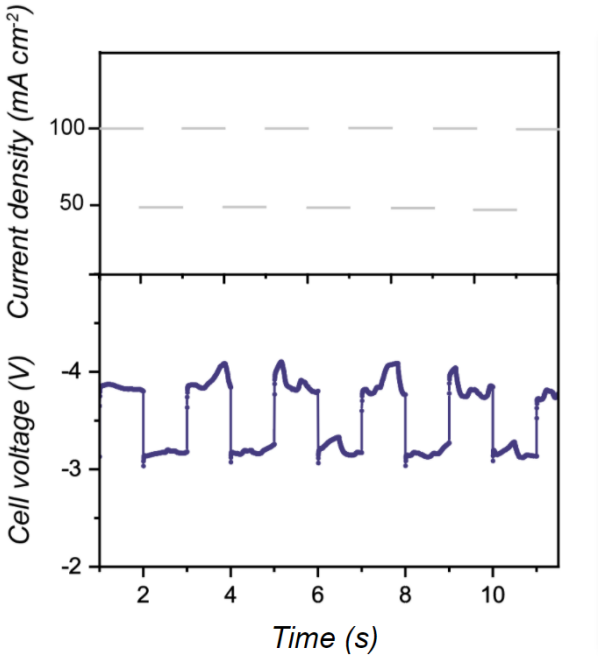

Fig. S24. Cell voltage response to a square-wave current density (100 mA cm^{-2} for 1 s followed by 50 mA cm^{-2} for 1 s) applied to the CO_2 electrolyzer when removing accumulated bubbles (after 4 h of electrolysis at 100 mA cm^{-2}). These plots correspond to the experiment performed in Figure 6 of the main text.

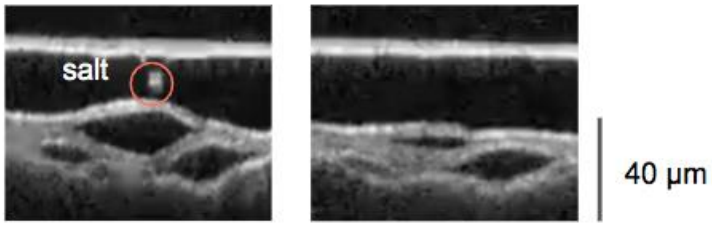

Fig. S25. An intensity image captured 4 h into Movie S1 shows the detection of a solid consistent with salt formation (left). The potential salt formation disappears in the next frame, 10 μs later (right).

Table S1. The light properties detected from electrolysis optical coherence tomography (eOCT) [Exp (CO_2), Exp (CO) and Exp (H_2)], [control (CO_2) and control (H_2)] and Ref (*32*) .

Gaseous species	Differential depolarization index (DDI)	ΔDDI	Anisotropy	Linear di-attenuation
Exp (CO_2)	2.9720	1.0097	0.2782	0.1969
Ref (CO_2)	4.03*	1.00	0.2664	0.1762
Control (CO_2)	2.9627	1.1889	0.2833	0.1771
Exp (CO)	1.7344	0.7397	0.0945	0.1460
Ref (CO)	0.48*	0.50	0.0897	0.1288
Control (CO)	-	-	-	-
Exp (H_2)	0.6645	0.2489	0.1345	0.0931
Ref (H_2)	0.32*	0.50	0.1280	0.0901
Control (H_2)	0.6084	0.1971	0.1392	0.0885

* The depolarization ratio from Ref (32) has a similar physical meaning with DDI (Section S3A) but in different scales.

S6. Supporting References and Notes

1. F. K. Ko, Y. Wan, *Introduction to Nanofiber Materials* (Cambridge University Press, 2014).

2. Electrospinning for advanced energy storage applications, (available at https://www.springer.com/gp/book/9789811588433).

3. X. Lu, H. Qu, M. Skorobogatiy, Piezoelectric Micro- and Nanostructured Fibers Fabricated from Thermoplastic Nanocomposites Using a Fiber Drawing Technique: Comparative Study and Potential Applications. *ACS Nano*. **11**, 2103–2114 (2017).

4. S. Ren, D. Joulié, D. Salvatore, K. Torbensen, M. Wang, M. Robert, C. P. Berlinguette, Molecular electrocatalysts can mediate fast, selective CO_2 reduction in a flow cell. *Science*. **365**, 367–369 (2019).

5. E. W. Lees, M. Goldman, A. G. Fink, D. J. Dvorak, D. A. Salvatore, Z. Zhang, N. W. X. Loo, C. P. Berlinguette, Electrodes Designed for Converting Bicarbonate into CO. *ACS Energy Lett.*, 2165–2173 (2020).

6. N. Ortega-Quijano, J. L. Arce-Diego, Depolarizing differential Mueller matrices. *Opt. Lett.* **36**, 2429–2431 (2011).

7. R. Clark Jones, A New Calculus for the Treatment of Optical SystemsI. Description and Discussion of the Calculus. *J. Opt. Soc. Am., JOSA*. **31**, 488–493 (1941).

8. N. A. Rubin, G. D'Aversa, P. Chevalier, Z. Shi, W. T. Chen, F. Capasso, Matrix Fourier optics enables a compact full-Stokes polarization camera. *Science*. **365** (2019), doi:10.1126/science.aax1839.

9. S. N. Savenkov, "Mueller Matrix Polarimetry in Material Science, Biomedical and Environmental Applications" in *Handbook of Coherent-Domain Optical Methods: Biomedical Diagnostics, Environmental Monitoring, and Materials Science*, V. V. Tuchin, Ed. (Springer New York, New York, NY, 2013), pp. 1175–1253.

10. G. Yao, L. V. Wang, Two-dimensional depth-resolved Mueller matrix characterization of biological tissue by optical coherence tomography. *Opt. Lett.* **24**, 537–539 (1999).

11. V. V. Tuchin, Polarized light interaction with tissues. *J. Biomed. Opt.* **21**, 71114 (2016).

12. J. J. Gil, R. Ossikovski, *Polarized Light and the Mueller Matrix Approach* (CRC Press, 2017).

13. M. Yamanari, M. Mase, R. Obata, M. Matsuzaki, T. Minami, S. Takagi, M. Yamamoto, N. Miyamoto, K. Ueda, N. Koide, T. Maeda, K. Totani, N. Aoki, Y. Hirami, S. Sugiyama, M. Mandai, M. Aihara, M. Takahashi, S. Kato, Y. Kurimoto, Melanin concentration and depolarization metrics measurement by polarization-sensitive optical coherence

tomography. *Sci. Rep.* **10**, 19513 (2020).

14. P. Beckmann, *The Depolarization of Electromagnetic Waves* (Golem Press, 1968).

15. Germer, Thomas A. Depolarization in diffusely scattering media. *Polarized Light and Optical Angular Momentum for Biomedical Diagnostics*. Vol. 11646. SPIE, 2021.

16. Azzam, R. M. A. (1978). Photopolarimetric measurement of the Mueller matrix by Fourier analysis of a single detected signal. *Opt. Lett.* **2**, 148-150 (1978).

17. R. Ossikovski, V. Devlaminck, General criterion for the physical realizability of the differential Mueller matrix. *Opt. Lett*. **39**, 1216 (2014).

18. V. Devlaminck, P. Terrier, J.-M. Charbois, Differential matrix physically admissible for depolarizing media: the case of diagonal matrices. *Opt. Lett.* **38**, 1497–1499 (2013).

19. B. N. Simon, S. Simon, N. Mukunda, F. Gori, M. Santarsiero, R. Borghi, R. Simon, A complete characterization of pre-Mueller and Mueller matrices in polarization optics. *J. Opt. Soc. Am. A Opt. Image Sci. Vis.* **27**, 188–199 (2010).

20. D. Huang, E. A. Swanson, C. P. Lin, J. S. Schuman, W. G. Stinson, W. Chang, M. R. Hee, T. Flotte, K. Gregory, C. A. Puliafito, J.G. Fujimoto, Optical coherence tomography. *Science*. **254**, 1178–1181 (1991).

21. V. Jayaraman, G. D. Cole, M. Robertson, C. Burgner, D. John, A. Uddin, A. Cable, Rapidly swept, ultra-widely-tunable 1060 nm MEMS-VCSELs. *Electron. Lett.* **48**, 1331–1333 (2012).

22. I. Grulkowski, J. J. Liu, B. Potsaid, V. Jayaraman, C. D. Lu, J. Jiang, A. E. Cable, J. S. Duker, J. G. Fujimoto, Retinal, anterior segment and full eye imaging using ultrahigh speed swept source OCT with vertical-cavity surface emitting lasers. *Biomed. Opt. Express*. **3**, 2733–2751 (2012).

23. M. Yamanari, S. Uematsu, K. Ishihara, Y. Ikuno, Parallel detection of Jones-matrix elements in polarization-sensitive optical coherence tomography. *Biomed. Opt. Express*. **10**, 2318–2336 (2019).

24. H. H. Hopkins, G. P. Thomson, The concept of partial coherence in optics. *Proc. R. Soc. Lond. A Math. Phys. Sci.* **208**, 263–277 (1951).

25. J. Bertolotti, O. Katz, Imaging in complex media. *Nat. Phys.* **18**, 1008–1017 (2022).

26. N. Ortega-Quijano, F. Fanjul-Vélez, J. L. Arce-Diego, Physically meaningful depolarization metric based on the differential Mueller matrix. *Opt. Lett.* **40**, 3280–3283 (2015).

27. M. Yamanari, S. Tsuda, T. Kokubun, Y. Shiga, K. Omodaka, N. Aizawa, Y. Yokoyama, N. Himori, S. Kunimatsu-Sanuki, K. Maruyama, H. Kunikata, T. Nakazawa, Estimation of Jones matrix, birefringence and entropy using Cloude-Pottier decomposition in polarization-

sensitive optical coherence tomography. *Biomed. Opt. Express*. **7**, 3551–3573 (2016).

28. N. Ortega-Quijano, T. Marvdashti, A. K. Ellerbee Bowden, Enhanced depolarization contrast in polarization-sensitive optical coherence tomography. *Opt. Lett.* **41**, 2350–2353 (2016).

29. R. A. Leitgeb, B. Baumann, Multimodal Optical Medical Imaging Concepts Based on Optical Coherence Tomography. *Front. Phys*. **6** (2018), doi:10.3389/fphy.2018.00114.

30. W. G. Egan, T. Hilgeman, J. Reichman, Determination of absorption and scattering coefficients for nonhomogeneous media. 2: experiment. *Appl. Opt.* **12**, 1816–1823 (1973).

31. B. Mandracchia, Z. Wang, V. Ferraro, M. M. Villone, E. Di Maio, P. L. Maffettone, P. Ferraro, Quantitative imaging of the complexity in liquid bubbles' evolution reveals the dynamics of film retraction. *Light: Science & Applications*. **8**, 1–12 (2019).

32. N. J. Bridge, A. D. Buckingham, J. W. Linnett, The polarization of laser light scattered by gases. *Proc. R. Soc. Lond. A Math. Phys. Sci.* **295**, 334–349 (1966).

33. A. Kokhanovsky, *Springer Series in Light Scattering: Volume 2: Light Scattering, Radiative Transfer and Remote Sensing* (Springer, 2017).

34. *Soviet Astronomy* (American Institute of Physics., 1991).

35. R. Shi, J. Guo, X. Zhang, G. I. N. Waterhouse, Z. Han, Y. Zhao, L. Shang, C. Zhou, L. Jiang, T. Zhang, Efficient wettability-controlled electroreduction of CO2 to CO at Au/C interfaces. *Nat. Commun.* **11**, 3028 (2020).

36. D. W. Oxtoby, W. M. Gelbart, Depolarized light scattering near the gas-liquid critical point. *J. Chem. Phys.* **60**, 3359–3367 (1974).

37. T. Fabritius, R. Myllylä, Investigation of swelling behaviour in strongly scattering porous media using optical coherence tomography. *J. Phys. D Appl. Phys.* **39**, 2609 (2006).

38. S. Tammina. Transfer learning using vgg-16 with deep convolutional neural network for classifying images. *Int. J. Sci. Res.* 143-150 (2019).

39. J. L. Puga, M. Krzywinski, N. Altman, Bayes' theorem. *Nat. Methods*. **12**, 277–278 (2015).

40. K. P. Murphy, Naive Bayes classifiers (2006), (available at https://www.ic.unicamp.br/~rocha/teaching/2011s1/mc906/aulas/naive-bayes.pdf).

41. J.D.M. Rennie, L. Shih, J. Teevan, D.R Karger. Tackling the Poor Assumptions of Naive Bayes Text Classifiers. In Proceedings of the Twentieth International Conference on Machine Learning. 616-623 (2003).

42. R. van de Schoot, S. Depaoli, R. King, B. Kramer, K. Märtens, M. G. Tadesse, M. Vannucci, A. Gelman, D. Veen, J. Willemsen, C. Yau, Bayesian statistics and modelling.

Nat. Rev. Methods Primers. **1**, 1–26 (2021).

43. G. M. Oliveira, A. Oravecz, D. Kobi, M. Maroquenne, K. Bystricky, T. Sexton, N. Molina, Precise measurements of chromatin diffusion dynamics by modeling using Gaussian processes. *Nat. Commun.* **12**, 6184 (2021).

44. F. P. G. de Arquer, C.-T. Dinh, A. Ozden, J. Wicks, C. McCallum, A. R. Kirmani, D.-H. Nam, C. Gabardo, A. Seifitokaldani, X. Wang, Y. C. Li, F. Li, J. Edwards, L. J. Richter, S. J. Thorpe, D. Sinton, E. H. Sargent, CO_2 electrolysis to multicarbon products at activities greater than 1 A cm^{-2}. *Science*. **367**, 661–666 (2020).

45. G. Wen, B. Ren, X. Wang, D. Luo, H. Dou, Y. Zheng, R. Gao, J. Gostick, A. Yu, Z. Chen, Continuous CO2 electrolysis using a CO2 exsolution-induced flow cell. *Nature Energy*. **7**, 978–988 (2022).

46. T. Michioka, S. Komori, Large-Eddy simulation of a turbulent reacting liquid flow. *AIChE J.* **50**, 2705–2720 (2004).

47. E. W. Lees, J. C. Bui, D. Song, A. Z. Weber, C. P. Berlinguette, Continuum Model to Define the Chemistry and Mass Transfer in a Bicarbonate Electrolyzer. *ACS Energy Lett.*, 834–842 (2022).

48. X. Lu, T. M. M. Heenan, J. J. Bailey, T. Li, K. Li, D. J. L. Brett, P. R. Shearing, Correlation between triple phase boundary and the microstructure of Solid Oxide Fuel Cell anodes: The role of composition, porosity and Ni densification. *J. Power Sources*. **365**, 210–219 (2017).

49. A. Bertei, E. Ruiz-Trejo, K. Kareh, V. Yufit, X. Wang, F. Tariq, N. P. Brandon, The fractal nature of the three-phase boundary: A heuristic approach to the degradation of nanostructured solid oxide fuel cell anodes. *Nano Energy*. **38**, 526–536 (2017).

50. N. Altman, M. Krzywinski, Simple linear regression. *Nat. Methods*. **12**, 999–1000 (2015).